SYNTHESIS AND ASSEMBLY OF MONODISPERSE ANISOMETRIC COLLOIDS

A Dissertation

Presented to the Faculty of the Graduate School

of Cornell University

In Partial Fulfillment of the Requirements for the Degree of

Doctor of Philosophy

by

Hsiaoyu Stephanie Lee

May 2009

SYNTHESIS AND ASSEMBLY OF MONODISPERSE ANISOMETRIC COLLOIDS

Hsiaoyu Stephanie Lee, Ph. D.

Cornell University 2009

The synthesis and assembly of anisometric colloids (500 nm to ~2 μm) have attracted recent interest from both a fundamental, as well as a technological standpoint. Computational simulations predict that these building blocks are capable of forming structures considerably more complex than those of their spherical counterparts. At the same time, emerging studies indicate that the resulting assemblies can possess striking properties such as negative refraction, despite the tendency for these materials to exhibit only partial order.

In this dissertation, I describe our efforts to understand how specific colloidal features on a single particle level can lead to a significant impact on their self-assembly behavior. One aspect of this work is the synthesis of a class of nonspherical core-shell and hollow particles, which can be directed into new colloidal phases by shape programming alone, by optical manipulation, or by magnetic fields. With these colloids as a platform, a number of unusual structures were then studied under confinement via real-time optical microscopy and videography.

Using hard peanut-shaped silica shells, we directly observed a 2D aperiodic ‘degenerate crystal’, described only in simulations to date. In this phase each of the constituent particle lobes occupies a triangular lattice site, while the dimer axes orient along one of the three underlying crystalline directions. Remarkably, we illustrate that an oblique crystal with orientational order can assemble instead, when hematite-silica

core-shell particles with the exact same shape are used. In this case, the canted antiferromagnetism of the core hematite, in conjunction with the hierarchical colloidal microstructure, produces a permanent transverse magnetic dipole in the dimers. This has the effect of introducing attractive dipolar forces to the interparticle potential. We also explored the structures formed by mildly-fused polystyrene-silica asymmetric dimers confined to gap heights intermediate to the in-plane monolayer and the out-of-plane monolayer. The system was found to evolve from a 2D (planar) oblique phase to a quasi-2D rotator, and finally to a 2D (upright) hexagonally-close-packed crystal. These studies highlight the rich phase behavior of complex dispersions, and show promise for diverse colloidal structures to be formed using simple self-assembly approaches to condense the systems.

BIOGRAPHICAL SKETCH

Hsiaoyu (Stephanie) was born in Taiwan on March 25th, 1981 and immigrated with her family to Toronto, Canada at the age of 7. She majored in Engineering Science, graduating with Honours from the inaugural class of the nanoengineering program at the University of Toronto. Her first research position was held in the laboratory of Dr. Honghi N. Tran (Chemical Engineering), where she investigated the effect of ash particle size and liquid content on the removability of deposits in entrained flow reactors. Stephanie also spent a summer as an intern at the Sunnybrook Health Sciences Centre (Imaging Research) under the guidance of Dr. Peter N. Burns. There, she explored the feasibility of drug delivery using an ultrasound-mediated approach *in vitro*. She moved to Ithaca, NY in August 2003 to continue her studies at Cornell University in the Department of Materials Science & Engineering. After rotating through various labs on campus as a Presidential Life Sciences Fellow, Stephanie joined the research group of Professor Chekesha M. Liddell in June 2004. During the past five years she has explored the role that single particle engineering plays on the self-assembly behavior of complex nonspherical colloids. She will move to Tokyo upon completing her degree, to conduct research as a Japan Society for the Promotion of Science (JSPS) Postdoctoral Fellow in Dr. Kazunori Kataoka's laboratory.

To my parents, who put their children

above all else.

ACKNOWLEDGMENTS

A great number of people have influenced my life and helped me to reach this goal. First, I would like to thank my advisor Prof. Chekesha Liddell, whose genuine interest to teach and cultivate was always appreciated. I also would like to thank my committee members, Prof. Frank DiSalvo and Prof. Uli Wiesner, for their support and assistance, and Prof. Lara Estroff and Prof. David Grubb for graciously serving as a proxy member for my candidacy and doctoral defense exams.

To all members, past and present, of the Liddell group – thanks for making the lab so enjoyable; it was a pleasure and privilege. A special thanks to my talented undergraduate students: Victoria, Isa, Amy, Stephanie, Jerry, Stephen, Dan, Esther, and Erin; I would not know about the 'real' world, or the latest buzz, without you. I hope you learned as much as I have learnt from you. Many thanks to my collaborators: Sharon Gerbode, Bettina John, Prof. Itai Cohen, and Prof. Fernando Escobedo for the always insightful discussion, tips on clean manuscript writing, and crazy ideas. Thanks as well to the Cohen group, whose lab was like a second home; to the facility managers of the Cornell Center of Materials Research (Mick, John Grazul, Maura, John Hunt) for training and technical expertise; and to the Bard Hall office staff (Joseph, Patty, Michele, Carol, Dolores, Vicki, Verne, and Laura) for your kindness.

Finally, I thank my family and friends for always being there, listening, and putting up with my idiosyncracies. To Marleen, Poorna, Baski, and Jared, whose loyalty and antics I will never forget; to Marion, for dedicatedly calling me long-distance despite my elusiveness; to my friends in Canada – Philip, Nir, Pat, Anne, and Tammy, for the comforting conversations; and to my friends in Ithaca – you have made the entire experience worthwhile. Duane, thank you for *everything*, not the least of which includes my daily lunch surprise.

TABLE OF CONTENTS

LIST OF FIGURES

CHAPTER 1

INTRODUCTION

Colloids and colloidal assemblies: a perspective

The field of colloid science has had a long history of importance in technology and the materials industry, spanning from its use as pigments in ancient inks to modern biotechnology. By definition, a colloidal suspension consists of solid particles dispersed in a continuous (liquid) medium, and is considered stable if it does not flocculate or settle due to sedimentation. Over the past few decades microscopic particles (500 nm to ~2 μm) have provided fascinating models for some basic but intriguing physics; for instance, they were instrumental to advances in the understanding of phase transitions,[1-5] crystallization kinetics,[6-8] and the problem of nucleation and growth (Figure 1.1).[9,10] In these cases the colloidal particles serve as analogues to 'atoms', since their phase behavior often mimics that of simple atomic liquids and solids. Yet, they undergo stochastic Brownian motion on a time scale accessible to experimental observation, and can be directly imaged via optical techniques due to their size. A comparison of molecular (atomic) and colloidal interactions is shown in Figure 1.2, using a Lennard-Jones potential for the former and a Derjaguin-Landau-Verwey-Overbeek (DLVO) potential for the latter.[10] At a surface potential of 30 mV and a Debye length of ~13 nm, the colloids show a comparable range and magnitude in their pair-wise interactions to atomic and molecular systems.

Ordered arrays of particles – or colloidal assemblies – can also show promise in applications such as optical computing elements,[11] quantitative chemical sensors,[12] or selectively permeable drug delivery vehicles,[13] among others. These colloidal structures acquire unique and useful properties not only from their constituent

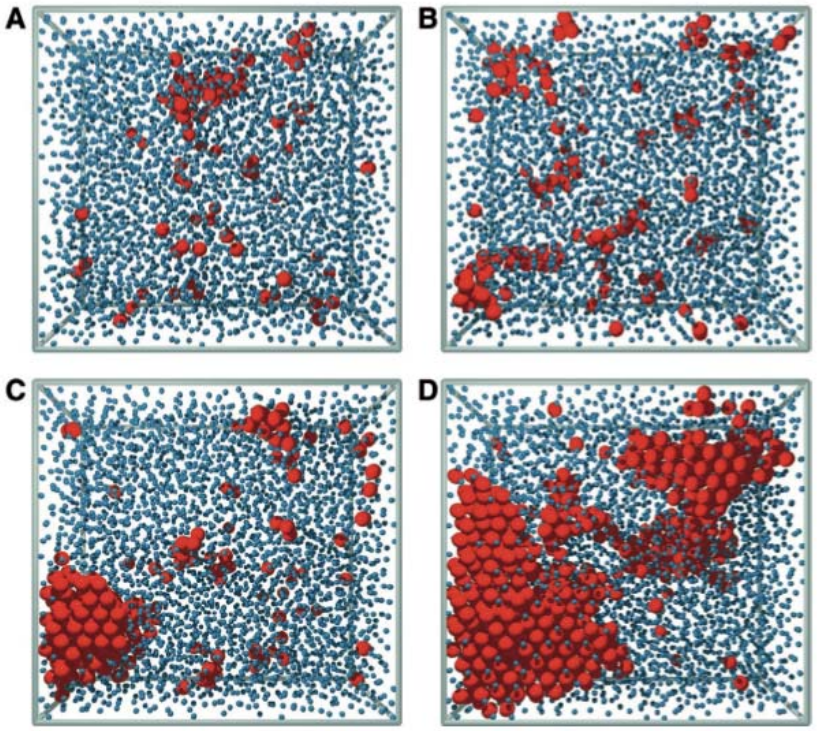

Figure 1.1. Four time snapshots during colloidal crystallization at a volume fraction of $\Phi = 0.45$. The red spheres are drawn to scale and represent crystal-like particles, while the blue spheres (reduced in size) represent particles in the metastable liquid state. Reproduced from reference 9.

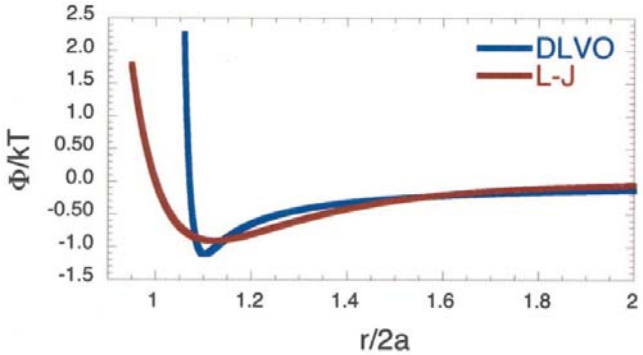

Figure 1.2. Comparison of the molecular (atomic) Lennard-Jones potential to a colloidal DLVO potential (at the secondary minimum / surface potential, 30 mV; Debye length, ~13 nm) for 1 μm polystyrene particles. The pair potentials are normalized by the thermal energy k_BT. The separation distances are normalized by the atomic and colloidal particle diameter, $2a$. Reproduced from reference 10.

materials but also from the spontaneous emergence of mesoscopic order.[14] A remarkable idea is that although colloidal assemblies typically form phases similar to atomic systems, they can under certain conditions display *greater* structural diversity. For example, in ionic colloidal crystals the stoichiometry was not restricted by charge neutrality, due to a 'buffering' effect in the electric double layer and free ions in solution.[15] As a result LS- and LS_6-type structures were observed, in addition to the rock salt CsCl structure (Figure 1.3). A similar diversification was seen in binary nanoparticle superlattices, where CuAu, $MgZn_2$, Fe_4C, $CaCu_5$, CaB_6, and $NaZn_{13}$-type phases were found.[16]

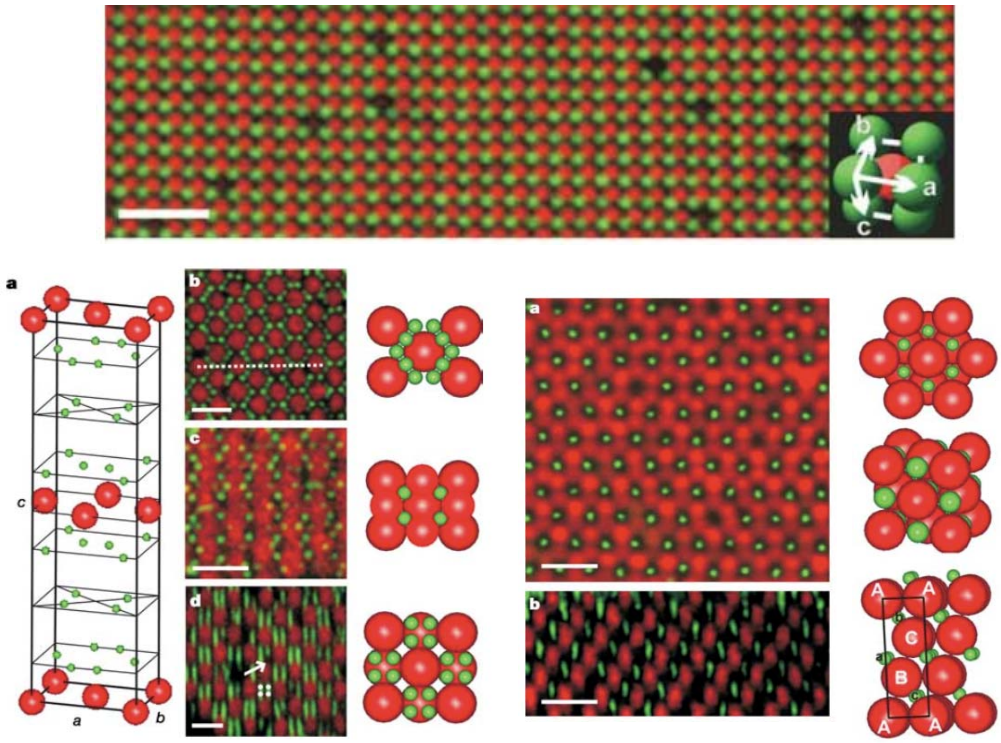

Figure 1.3. Ionic colloidal crystals of the rock salt CsCl structure (top, scale bar 10 μm), and non-stoichiometric LS-type structure (bottom left, all scale bar 4 μm), and LS_6-type structure (bottom right, all scale bar 8 μm). Reproduced from reference 15.

Why anisotropic particles?

The colloidal particles described to this point have all been isotropic, whether in shape or interaction. The impressive range of structures seen in the binary systems were possible because added complexities (i.e., in particle size and surface charge) allowed phases to evolve from the common structures associated with the packing of spheres – that is, the random hexagonally-close-packed, or face-centered-cubic crystals. In the submicron- and micron- size regime, surface tension in wet chemical syntheses tends to favor the formation of spherical colloids. However, new progress in this field has now produced a vast array of options[17] ranging from Janus (i.e., two-faced, or surface anisotropic)[18-23] and 'patchy' (i.e., locally functionalized) particles,[24,25] to nonspherical particles (Figure 1.4).[26-47] Chemical methods developed include emulsion-based,[33-35] seeded polymerization,[38-43] inorganic,[36,37] or clusterization processes,[28-32] while physical methods include microcontact printing,[18,19] microfluidic,[20,21] or particle lithography techniques.[25,26,44-47]

An exciting aspect of these advances is the recognition that anisotropic shape and interactions can enable breakthroughs for the assembly of targeted materials.[49] Colloids with 4-fold valence, which resemble *sp3* hybridized chemical bonds,[50] have the potential to assemble into the diamond structure so desirable for omnidirectional photonic bandgaps.[51,52] At the same time, nonspherical building blocks are predicted to form unusual or non-close-packed phases intermediate to liquids (with no translational order) and crystals (with long-range periodicity).[53] These include liquid crystalline phases (nematic, smectic-A, etc.), rotator or plastic crystals, aperiodic or degenerate crystals, and base-centered monoclinic crystals.[54-56] Although a few of these phases exhibit only partial order, emerging studies indicate that they may possess interesting functional properties i.e., superlensing behavior in a flat lens.[57]

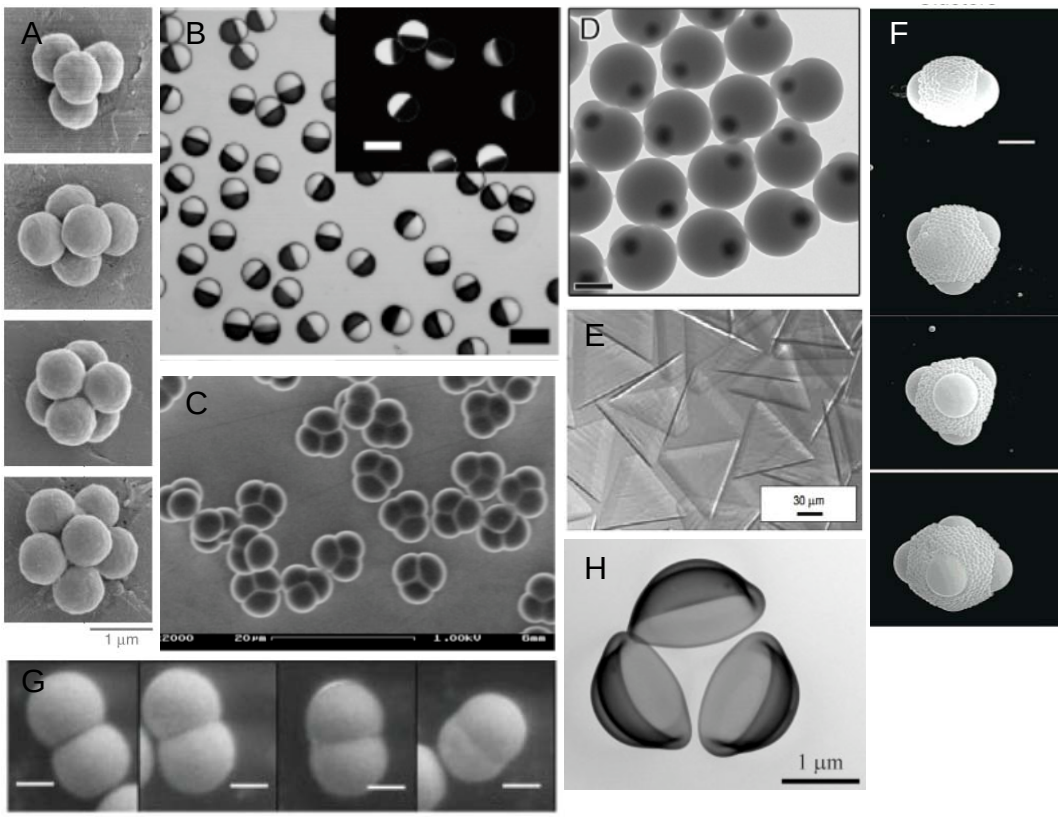

Figure 1.4. Innovative syntheses of complex colloidal particles in recent years (i.e., Janus, patchy, nonspherical, dipolar). Reproduced from references 33, 20, 40, 41, 26, 34, 31, and 48 (parts A through H, respectively).

Progress in anisotropic colloidal assembly, on the other hand, has significantly lagged with respect to the synthesis domain. The challenges here are a reliance on the availability of appropriate building blocks of sufficient monodispersity and yield, in addition to the difficulty in controlling the many forces simultaneously acting on colloidal systems i.e., gravity, capillary, electrostatic, van der Waals, etc. A conceptually unifying framework with which to understand, classify, and describe various particles and their assemblies is also needed.[49] One well developed area in this pursuit is the class of electrorheological (magnetorheological) fluids,[58] which are spherical in shape, but dipolar (anisotropic) in interaction. There, the introduction of

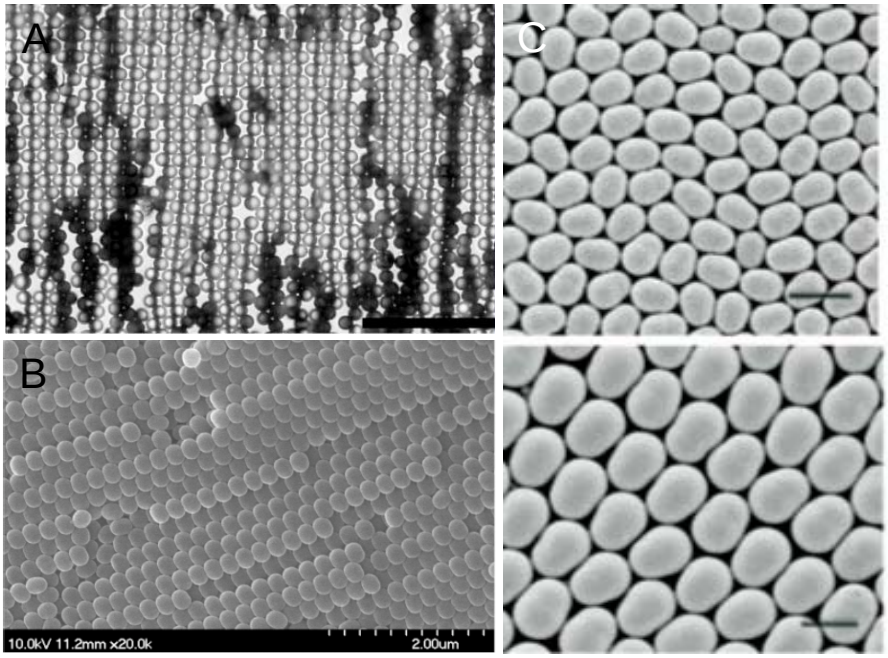

Figure 1.5. Different types of colloidal assemblies from a) Janus-type metallodielectric spheres, b) spherocylinder-type dimers and c) asymmetric dimers. Reproduced from references 59, 65, and 64 (parts A through C, respectively).

anisotropy expands the possible phases as expected, to include predominantly chains and occasional tetragonal structures.[6] Interesting 2D zigzag arrays were also shown for Janus particles under AC electric and magnetic fields (Figure 1.5a).[59,60] For nonspherical particles with hard-body interactions, recent assembly has been performed using evaporation-induced convective assembly,[61-64] or in bulk with concentrated suspensions (Figure 1.5b,c).[65] These early reports hint at the revolutionary materials that can be acquired from nonspherical particle assembly, and show great promise to form a rich number of complex structures.

Thesis overview

This dissertation focuses on nonspherical (anisometric) particles of a dimer-like morphology i.e., peanut-shaped colloids approximated by two spheres tangentially

connected, or asymmetric dimers well characterized by two interpenetrating spheres of unequal radii. We describe their synthesis and assembly, and demonstrate how the specific features of the individual colloids contribute to dramatically different self-assembly behavior. The systems are investigated using real-space optical microscopy and videography, with the majority of the assemblies formed under strictly 2D confinement.

The outline of the thesis is as follows: in Chapter 2 we introduce the peanut-shaped colloidal system and provide synthesis details of the various architectures (core-shell, hollow) and materials (core: hematite α-Fe_2O_3 / shell: SiO_2, TiO_2, and ZnS).[66] By selective dissolution of the core, hollow silica and titania shells were produced with refractive indices sufficient for trapping and localization using holographic optical tweezers. Magnetic functionality was also incorporated into core-shell colloids by reducing the iron oxide, which allowed for control of the particle orientations via external fields. The result was the assembly of nematic-type phases with both in-plane and out-of-plane orientational order. In Chapter 3 we use a fluorescently-labeled version of the hollow silica shells under confinement to investigate the effects of self-assembly based only on shape. A 2D aperiodic degenerate crystal (DC) was observed for the first time[67] since its proposal by Wojciechowski in 1987.[68] In the DC, constituent peanut lobes decorate a triangular lattice while orientations align along one of three crystalline directions. The centers of mass sparsely decorate a *kagomé* lattice. To explore the implications of lobe pairing on structural ordering, we compared Monte Carlo simulations of defect annealing in monomer versus dimer systems. Our results suggest that DCs exhibit restricted dislocation and defect dynamics, which may yield material properties such as novel auxetic (negative Poisson's ratio) behavior.[69] Chapter 4 extends the assembly efforts of the peanut-shaped particles by using the unprocessed hematite-silica core-shell

particles instead of the hollow SiO_2 shells. Due to hematite's hierarchical microstructure and antiferromagnetic properties, this set of particles contained a permanent transverse magnetic dipole (i.e., oriented along the short axis). The combination of this magnetic anisotropy, along with the peanut-like shape, allowed for the formation of complex structures including crisscrossed chains, as well as a 2D oblique crystal with the *p2* plane group symmetry. Several notable features of these building blocks are: (1) a high degree of orientational order (2) positional ordering within one chain i.e., due to shape complementarity, and (3) a highly selective side-to-side interaction. The final chapter of the dissertation describes the synthesis and assembly of asymmetric polystyrene-silica colloids of a mildly-fused geometry. We explored the two possible monolayer structures in this system i.e., in an in-plane oblique crystal versus an out-of-plane hexagonally-close-packed phase. Strikingly, a quasi-2D rotator state (in which particle centers-of-mass roughly lie on a triangular lattice, but have complete orientational freedom) at confinement heights intermediate to these two regimes was found. This structure was possible only when slight out-of-plane motion was allowed. Thus, our results reinforce the idea that confinement (free volume) is critical in colloidal assembly, just as in broader molecular systems such as block-copolymer melts in thin films.

REFERENCES

1. E. R. Weeks, J. C. Crocker, A. C. Levitt, A. Schofield and D. A. Weitz. *Science*,**287**, 627 (2000).

2. W. C. K. Poon, *MRS Bulletin*, **29**, 96 (2004).

3. R. P. A. Dullens, *Soft Matter*, **2**, 805 (2006).

4. P. N. Pusey and W. van Megen. *Nature*, **320**, 340 (1986).

5. Y. Monovoukas and A. P. Gast. *Journal of Colloid and Interface Science*, **128**, 533 (1989).

6. A. Yethiraj and A. van Blaaderen. *Nature*, **421**, 513 (2003).

7. V. J. Anderson and H. N. W. Lekkerkerker. *Nature*, **416**, 811 (2002).

8. W. van Megen and S. M. Underwood. *Nature*, **362**, 616 (1993).

9. U. Gasser, E. R. Weeks, A. Schofield, P. N. Pusey and D. A. Weitz. *Science*, **292**, 258 (2001).

10. S. C. Glotzer, M. J. Solomon and N. A. Kotov. *AiChE Journal*, **50**, 2978 (2004).

11. A. Arsenault, S. Fournier-Bidoz, B. Hatton, H. Miguez, N. Tetreault, E. Vekris, S. Wong, S. M. Yang, V. Kitaev and G. A. Ozin. *Journal of Materials Chemistry*, **14**, 781 (2004).

12. J. H. Holtz and S. A. Asher. *Nature*, **389**, 829 (1997).

13. A. D. Dinsmore, M. F. Hsu, M. G. Nikolaides, M. Marquez, A. R. Bausch and D. A. Weitz. *Science*, **298**, 1006 (2002).

14. D. G. Grier. *MRS Bulletin*, **23**, 21 (1998).

15. M. E. Leunissen, C. G. Christova, A. P. Hynninen, C. P. Royall, A. I. Campbell, A. Imhof, M. Dijkstra, R. van Roij and A. van Blaaderen. *Nature*, **437**, 235 (2005).

16. E. V. Shevchenko, D. V. Talapin, N. A. Kotov, S. O'Brien and C. B. Murray. *Nature*, **439**, 55 (2006).

17. S. M. Yang, S. H. Kim, J. M. Lim and G. R. Yi. *Journal of Materials Chemistry*, **18**, 2177 (2008).

18. J. Q. Cui and I. Kretzschmar. *Langmuir*, **22**, 8281 (2006).

19. O. J. Cayre, V. N. Paunov and O. D. Velev. *Journal of Materials Chemistry*, **13**, 2445 (2003).

20. Z. Nie, W. Li, M. Seo, S. Xu and E. Kumacheva. *Journal of the American Chemical Society*, **128**, 9408 (2006).

21. K. H. Roh, D. C. Martin and J. Lahann. *Nature Materials*, **4**, 759 (2005).

22. M. A. Correa-Duarte, V. Salgueirino-Maceira, B. Rodriguez-Gonzalez, L. M. Liz-Marzan, A. Kosiorek, W. Kandulski and M. Giersig. *Advanced Materials*, **17**, 2014 (2005).

23. A. Perro, S. Reculusa, S. Ravaine, E. Bourgeat-Lami and E. Duguet. *Journal of Materials Chemistry*, **15**, 3745 (2005).

24. Y. S. Cho, G. R. Yi, S. H. Kim, S. J. Jeon, M. T. Elsesser, H. K. Yu, S. M. Yang and D. J. Pine. *Chemistry of Materials*, **19**, 3183 (2007).

25. L. Wang, L. Xia, G. Li, S. Ravaine and X. S. Zhao. *Angewandte Chemie International Edition*, **47**, 4725 (2008).

26. D. Dendukuri, D. C. Pregibon, J. Collins, T. A. Hatton and P. S. Doyle. *Nature Materials*, **5**, 365 (2006).

27. J. A. Champion, Y. K. Katare and S. Mitragotri. *Proceedings of the National Academy of Science*. **104**, 11901 (2007).

28. Y Yin and Y. Xia. *Advanced Materials*, **13**, 268 (2001).

29. M. Ibisate, Z. Zou and Y. Xia. *Advanced Functional Materials*, **16**, 1627 (2006).

30. A. M. Yake, R A. Panella, C. E. Snyder and D. Velegol. *Langmuir*, **22**, 9135 (2006).

31. C. M. Liddell and C. J. Summers. *Advanced Materials*, **15**, 1715 (2003).

32. P. M. Johnson, C. M. van Kats and A. van Blaaderen. *Langmuir*, **21**, 11510 (2005).

33. V. N. Manoharan, M. T. Elsesser and D. J. Pine. *Science*, **301**, 483 (2003).

34. Y. S. Cho, G. R. Yi, J. M. Lim, S. H. Kim, V. N. Manoharan, D. J. Pine and S. M. Yang. *Journal of the American Chemical Society*, **127**, 15968 (2005).

35. D. Zerrouki, B. Rotenberg, S. Abramson, J. Baudry, C. Goubault, F. Leal-Calderon, D. J. Pine and J. Bibette. *Langmuir*, **22**, 57 (2006).

36. S. Sacanna, L. Rossi, B. W. M. Kuipers and A. P. Philipse. *Langmuir*, **22**, 1822 (2006).

37. X. W. Lou and L. A. Archer. *Advanced Materials*, **20**, 1853 (2008).

38. H. R. Sheu, M. S. El-Aasser and J. W. Vanderhoff. *Journal of Polymer Science: Part A: Polymer Chemistry*, **28**, 653 (1990).

39. H. Minami, Z. Wang, T. Yamashita and M. Okubo. *Colloid and Polymer Science*, **281**, 246 (2003).

40. (a) J. W. Kim, R. J. Larsen and D. A. Weitz. *Journal of the American Chemical Society*, **128**, 14374 (2006); (b) J. W. Kim, R. J. Larsen and D. A. Weitz. *Advanced Materials*, **19**, 2005 (2005).

41. J. Ge, Y. Hu, T. Zhang and Y. Yin. *Journal of the American Chemical Society*, **129**, 8974 (2007).

42. D. Nagao, M. Hashimoto, K. Hayasaka and M. Konno. *Macromolecular Rapid Communications*, **29**, 1484 (2008).

43. E. B. Mock, H. De Bruyn, B. S. Hawkett, R. G. Gilbert and C. F. Zukoski. *Langmuir*, **22**, 4037 (2006).

44. C. Bae, J. Moon, H. Shin, J. Kim and M. M. Sung. *Journal of the American Chemical Society*, **129**, 14232 (2007).

45. C. E. Snyder, A. M. Yake, J. Feick and D. Velegol. *Langmuir*, **21**, 4813 (2005).

46. G. Zhang, D. Wang and H. Mohwald. *Angewandte Chemie International Edition*, **44**, 7767 (2005).

47. T. van Dillen, A. van Blaaderen and A. Polman. *Materials Today*, **7**, 40 (2004).

48. C. I. Zoldesi and A. Imhof. *Advanced Materials*, **7**, 924 (2005).

49. S. C. Glotzer and M. J. Solomon. *Nature Materials*, **6**, 557 (2007).

50. D. R. Nelson. *Nano Letters*, **2**, 1125 (2002).

51. Z. Zhang, A. S. Keys, T. Chen and S. C. Glotzer. *Langmuir*, **21**, 11547 (2005).

52. Y. Lu, Y. Yin and Y. Xia. *Advanced Materials*, **13**, 415 (2001).

53. M. P. Allen, G. T. Evans, D. Frenkel and B. M. Mulder. *Advances in Chemical Physics*, **86**, 1 (1993).

54. P. Bolhuis and D. Frenkel. *Journal of Chemical Physics*, **106**, 666 (1997).

55. T. Schilling, S. Pronk, B. Mulder and D. Frenkel. *Physical Review E*, **71**, 036138 (2005).

56. K. W. Wojciechowski, D. Frenkel and A. C. Branka. *Physical Review Letters*, **66**, 3168 (1991).

57. Z. Feng, X. Zhang, S. Feng, K. Ren, Z. Y. Li, B. Cheng and D. Zhang. *Journal of Optics A: Pure and Applied Optics*, **9**, 101 (2007).

58. H. Block and J. P. Kelly. *Journal of Physics D: Applied Physics*, **21**, 1661 (1988).

59. S. Gangwal, O. J. Cayre and O. D. Velev. *Langmuir*, **24**, 13312 (2008).

60. S. K. Smoukov, S. Gangwal, M. Marquez and O. D. Velev. *Soft Matter*, DOI: 10.1039/b814304h (2009).

61. I. D. Hosein and C. M. Liddell. *Langmuir*, **23**, 8810 (2007).

62. I. D. Hosein and C. M. Liddell. *Langmuir*, **23**, 10479 (2007).

63. J. A. Lee, L. Meng, D. J. Norris, L. E. Scriven and M. Tsapatsis. *Langmuir*, **22**, 5217 (2006).

64. I. D. Hosein, B. S. John, S. H. Lee, F. A. Escobedo and C. M. Liddell. *Journal of Materials Chemistry*, **19**, 344 (2009).

65. E. B. Mock and C. F. Zukoski. *Langmuir*, **23**, 8760 (2007).

66. S. H. Lee, Y. Song, I. D. Hosein and C. M. Liddell. *Journal of Materials Chemistry*, **19**, 350 (2009).

67. S. H. Lee, S. J. Gerbode, B. S. John, A. K. Wolfgang, F. A. Escobedo, I. Cohen and C. M. Liddell. *Journal of Materials Chemistry*, **18**, 4912 (2008).

68. K. W. Wojciechowski. *Physics Letters A*, **122**, 377 (1987).

69. K. V. Tretiakov and K. W. Wojciechowski. *Journal of Non-crystalline Solids*, **352**, 4221 (2006).

CHAPTER 2

MAGNETICALLY RESPONSIVE AND HOLLOW COLLOIDS FROM NONSPHERICAL CORE-SHELL PARTICLES OF PEANUT-LIKE SHAPE*

Colloids are attractive building blocks that show promise for the self-assembly of periodic and complex materials of technological interest.[1] Of these, particles with a core-shell architecture have been extensively explored in recent years, largely because of their ability to offer multifunctional properties when the core and shell chemistries are tuned independently of one another.[2,3] By engineering colloids on a single particle level, core-shell particles can often exhibit superior chemical (surface charge, surface area, reactivity) and physical (magnetic, optical) properties relative to single component systems. These enhancements include improved colloidal stability across a range of solvents, increased photocatalytic activity, corrosion resistance, or simultaneous cell targeting, drug delivery, and diagnostic imaging capabilities in nanoparticle-based therapeutics.[4] In quantum dots the photoluminescence quantum efficiency can also be greatly amplified by capping the core, i.e., CdSe, with an overlayer of a higher bandgap semiconductor material, i.e., ZnS.[5]

Strategies to uniformly coat dispersed particles can be broadly categorized into a few main classes[2]: (1) polymerization techniques (via surface condensation of monomers/coupling agents, microemulsions, etc.), (2) chemical vapor or atomic layer

---

* Originally Published as: Stephanie H. Lee, Yanning Song, Ian D. Hosein and Chekesha M. Liddell. "Magnetically responsive and hollow colloids from nonspherical core-shell particles of peanut-like shape", *J Mater Chem*, **19**, 350 (2009). *Reprinted by permission of The Royal Society of Chemistry*, http://www.rsc.org/Publishing/Journals/JM/article.asp?doi=b817844e.

deposition, (3) the layer-by-layer approach, (4) deposition or heterocoagulation with preformed colloids, (5) hydrolysis and condensation of metal alkoxides, and (6) precipitation of the coating material in a supersaturated solution. Using these methods a rich variety of coatings have been deposited onto spherical colloids to date. However, fewer accounts have described core-shell architectures of nonspherical particles in the micron and submicron size regime, predominantly because suitable templates have been more difficult to generate. These reports include the synthesis of 'egg-shell-like' hollow TiO_2,[6,7] α-Fe_2O_3@SiO_2@polypyrrole ellipsoidal sandwich composite particles,[8] double-walled SnO_2 "nano-cocoons" made using a hydrothermal shell-by-shell deposition,[9] and ellipsoidal Fe@SiO_2 spindles.[10] The relatively narrow choice of materials and shapes in nonspherical particle systems is a critical roadblock in colloid-based technologies requiring structures not easily accessible via the assembly of spheres. A prime example is diamond-type colloidal crystal structures formed by dimers on a face-centered cubic lattice, which may produce wide omni-directional photonic bandgaps when the refractive index contrast is sufficient.[11] Remarkably, the resulting bandgaps were predicted to be more tolerant of disorder arising from self-assembly processes than those associated with colloidal crystals made from spheres.[12]

Anisometric particles can also exhibit varied properties from their spherical counterparts based on their shape. For instance, Au nanocages synthesized from the galvanic replacement of sacrificial Ag nanocubes were found to be better optical absorbers than nanospheres made of the same material.[13] The absorption peak of the Au nanocages could be more precisely tuned than the nanospheres, making these particles powerful photothermal agents in cancer therapy, once conjugated with targeting monoclonal antibodies[13]. The increasing focus in colloid science on nonspherical systems also requires model particles from the perspective of

fundamental studies on the static and dynamic properties of concentrated dispersions. In this context, hollow fluorescent SiO_2 ellipsoids have recently been used to investigate the problem of rotational diffusion via fluorescence recovery after photobleaching.[14] The silica ellipsoids were also index matched to the suspension medium to extend their use to direct observations in 3D using a confocal laser scanning microscope.

Peanut-shaped colloids have been prepared by several groups[15-17] and used recently as sacrificial templates to create hollow shells that assembled into an aperiodic crystal structure.[18] The present work extends this scope and makes further functional, dimer-like particles available via the synthesis of monodisperse hematite (α-Fe_2O_3) colloids coated with inorganic shells of either ZnS, TiO_2, or SiO_2. In this scheme, both the uncoated and coated hematite cores can be easily converted to highly magnetic materials without loss of the nonspherical morphology. In the presence of an external magnetic field, peanut-shaped colloids align with their major axes parallel to the field direction, and assemble into thin films with particle orientational control upon slow drying. Hollow shells of silica and titania are also demonstrated after selective removal of the iron oxide core with an acid etch. We illustrate that the TiO_2 shells, with their high refractive index, can be suitably trapped using holographic optical tweezers.

Figure 2.1a shows a field emission scanning electron micrograph (FE-SEM) illustrating the highly monodisperse peanut-shaped hematite formed by the forced hydrolysis of a condensed $Fe(OH)_3$ gel in the presence of Na_2SO_4.[15] Each colloid is polycrystalline in nature and exhibits a particulate surface, as is evident from a high-magnification image of the hematite sample (Figure 2.1b). The overall nonspherical shape arises from a microstructure which consists of small, acicular crystallites that radiate outwards into two lobes from the particle center. This internal structure is

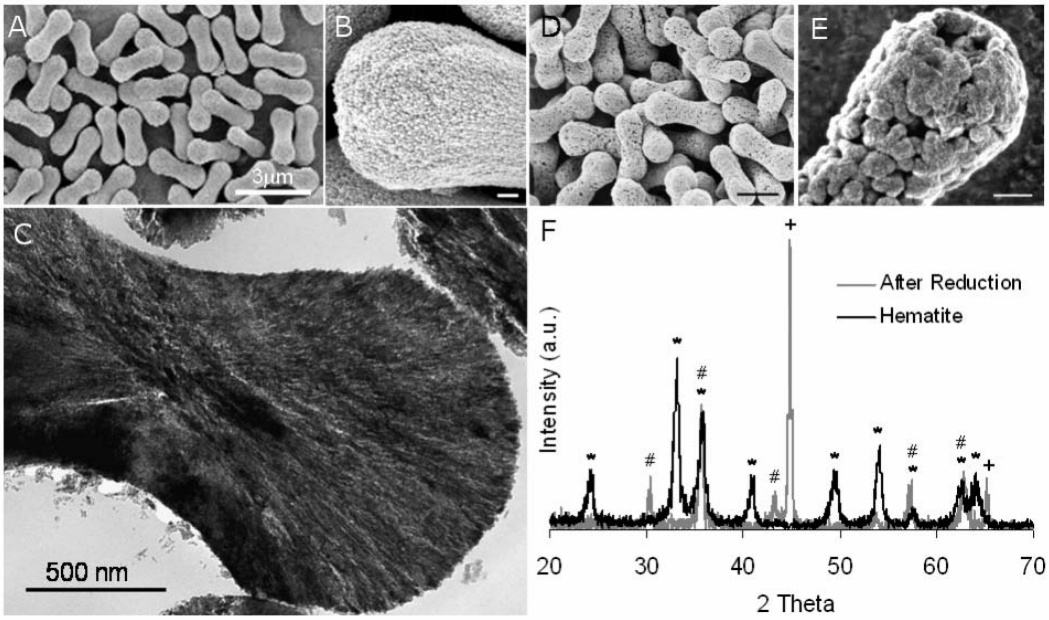

Figure 2.1. a) FE-SEM image of monodisperse hematite peanut-shaped particles. b) Close-up image of the hematite surface, which shows a particulate texture. Scale bar, 100 nm. c) Transmission electron micrograph of a hematite particle. This image clearly reveals acicular crystallites oriented preferentially along the particle major axis. d) FE-SEM image of hematite colloids after reduction into magnetite and iron. The morphology of the particles is preserved. Scale bar, 1 micron. e) High-magnification image of the reduced particles, illustrating the presence of large pores. Scale bar, 200 nm. f) X-ray diffraction patterns for the hematite (black) and reduced particles (grey). The original particles were indexed to JCPDS card no. 33-0664 (*), while the iron/magnetite particles were indexed to JCPDS card no. 06-0696 (+) and 19-0629 (#).

clearly revealed by a transmission electron micrograph (TEM) of a microtomed particle as shown in Figure 2.1c. By varying the SO_4^{2-} concentration it is possible to control the extent of splay and elongation in the acicular crystallites, and thus to critically influence the final particle shape. Indeed, dissociated sulfate ions were determined to adsorb to all crystal facets perpendicular to the [0001] axis of hematite, thereby hindering additions to those surfaces and causing the observed anisotropic crystallite growth.[15] The iron oxide particles measure 2.07 μm in length and 908 nm in lobe diameter (coefficient of variation, CV = 4.7% and 6.4%, respectively). X-ray powder diffraction (XRD) confirms that particles are single-phase α-Fe_2O_3 (JCPDS card no. 33-0664) with a mean crystallite size of 16 nm (Figure 2.1f), as calculated from the Scherrer equation using the (104) reflection at 33.2˚. When the hematite was reduced under H_2 at 300 ˚C for 3 hours, transformation into a mixture of iron (α-Fe) and magnetite (Fe_3O_4) (JCPDS card no. 06-0696 and no. 19-0629, respectively) was observed (Figure 2.1f). Figure 2.1d illustrates that colloids were successfully converted to the highly magnetic phases without loss of the nonspherical morphology. The as-formed colloids however, exhibited large pores and degradation in the acicular crystallite microstructure (Figure 2.1e). Here, it appears that the change from a rhombohedral (hematite) to the cubic (magnetite, iron) crystal systems caused internal restructuring, but on a local length scale which enabled the particles to preserve their overall peanut-like shape. It is likely that the phase transformation is surface-nucleated and proceeds with rather limited diffusion of both the iron and oxygen ions.[19]

The α-Fe_2O_3 core particles can be conformally coated with a number of inorganic materials without prior surface modification. In the case of silica, hydrolysis and condensation of a silicon alkoxide precursor under sonication produced smooth coatings (Figure 2.2a, 2.2d). No homogeneous silica nanoparticles were nucleated and the thickness of the amorphous SiO_2 shell was easily controlled by changing the

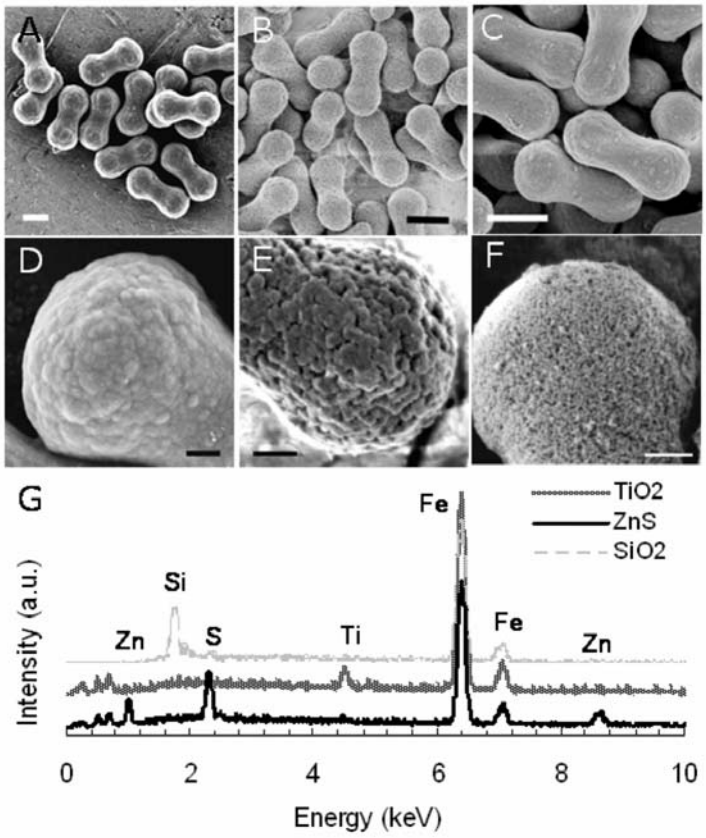

Figure 2.2. FE-SEM images of the coated hematite core-shell samples: a) After SiO_2 coating, b) ZnS coating, and c) TiO_2 coating. All three scale bars are 1 micron. d-f) High-magnification scanning electron micrographs of the corresponding SiO_2- , ZnS- and TiO_2-coated surfaces. Scale bar, 200 nm. g) EDS scan of the core-shell samples, indicating Fe as expected, along with Si, Ti, Zn, and S. Low energy peaks (<1 keV) are associated with elements such as O, C, etc.

reaction time. Although silica opens opportunities for a spectrum of surface functionalizations and is stable in a variety of aqueous and organic solvents, its low refractive index restricts its use in many optical applications. Thus, we also coated the peanut-shaped hematite with materials of high refractive index, including ZnS (n_{bulk} ~2.3) and TiO_2 (n_{bulk} ~2.5). The ZnS precipitates with thioacetamide decomposition in the presence of the metal salt, while the TiO_2 deposition proceeds via a sol-gel reaction. The FE-SEM images corresponding to these samples are shown in Figure 2.2b-c. A rough surface texture for both coatings is apparent from close inspection of Figure 2.2e-f. Since the sol-gel route produces amorphous materials, the XRD patterns from the three core-shell systems indicate only a crystalline signature modification (compared to bare hematite) in the α-Fe_2O_3-ZnS composite particles (supporting information). We observe the (111) reflection characteristic of the zinc blende, or sphalerite ZnS polymorph (JCPDS card no. 05-0556) at 28.6˚. Pronounced peak broadening results in a small calculated mean crystallite size of 4 nm. To confirm the elemental composition of the colloids, samples were also analyzed using energy-dispersive spectroscopy (EDS) as shown in Figure 2.2g. The three spectra reveal a strong signal from Fe as expected, with clear peaks from Zn, S, Ti, and Si for each of the corresponding core-shell samples. We note for the different coatings that peanut-shaped colloids were electrostatically-stabilized by suspending the particles at a pH value greater than their respective isoelectric points (IEP_{ZnS} ~ 3.0, IEP_{SiO2} ~2.5, IEP_{TiO2} ~5.5). Thus for the oxide shells, surface hydroxyl groups were negatively charged at pH 7 and helped to prevent particle aggregation.

Hematite (α-Fe_2O_3) is in general considered a poor magnetic material, especially when compared to the spinel ferrite forms of the iron oxides i.e., magnetite (Fe_3O_4), or iron itself. Below the Morin transition (T_M = 263K) hematite exhibits antiferromagnetic behavior, while between T_M and its Néel temperature (T_N = 948K) it

undergoes spin canting and becomes a weak ferromagnet[20] with a low spontaneous magnetization (M_s) value of 0.4 emu/g. On nano- and microscales (1 nm – 10 μm), this low M_s leads to relatively weak particle moment-applied field forces (torques), which may limit the utility of the hematite-based colloids in field-assisted assembly approaches (since order may be lost upon drying). To prepare core-shell particles with strong magnetic response, we reduced the α-Fe_2O_3-SiO_2, α-Fe_2O_3-TiO_2, and α-Fe_2O_3-ZnS colloids using the same method described for the plain hematite cores. Figure 2.3 illustrates the field-dependent magnetization curves from two samples of the SiO_2-coated particles, along with the uncoated iron/Fe_3O_4 cores, using vibrating sample magnetometry (VSM) at room temperature. Data was collected from random-orientation powder specimens after H_2 reduction at 300 ˚C for 3 hours. The hysteresis curve for the iron/Fe_3O_4 indicates ferromagnetic behavior with a coercivity (H_c) of 42 Oe and a respectable value of 91 emu/g for M_s. In the SiO_2-coated particles lower values of M_s were obtained with increasing coating time, since the silica shell does not contribute to the overall magnetic moment. Additionally, the value of H_c was increased to 210 Oe (4 hour coating), which is likely due to reduced diffusivity of H_2 through the thicker SiO_2 shell. The average crystallite size (d) was smaller here ($d_{magnetite}$ = 16 nm; d_{iron} = 23 nm) than in the uncoated particles ($d_{magnetite}$ = 28 nm; d_{iron} = 53 nm), suggesting a decrease in the rate of phase transformation and related grain growth. Since H_c is known to vary inversely with d,[21] the increase in coercivity appears to be consistent with the microstructural differences between the uncoated and coated samples. The magnetization curves for the ZnS- and TiO_2-coated colloids show similar trends of reduced M_s values but increased H_c. This data is included in the supporting information.

Under the influence of an external magnetic field, the colloids experience a torque which causes their major axes to align with the direction of the applied field.

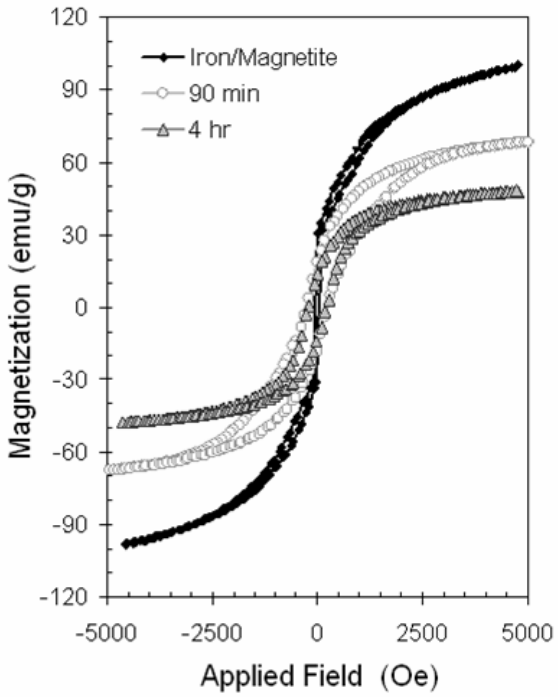

Figure 2.3. Vibrating sample magnetometer (VSM) measurement of the reduced samples at room temperature. Hysteresis curves are shown for the uncoated particles (black, closed circles), as well as particles coated with SiO_2 for 90 minutes (light grey, open circles) and 4 hours (grey, closed triangles).

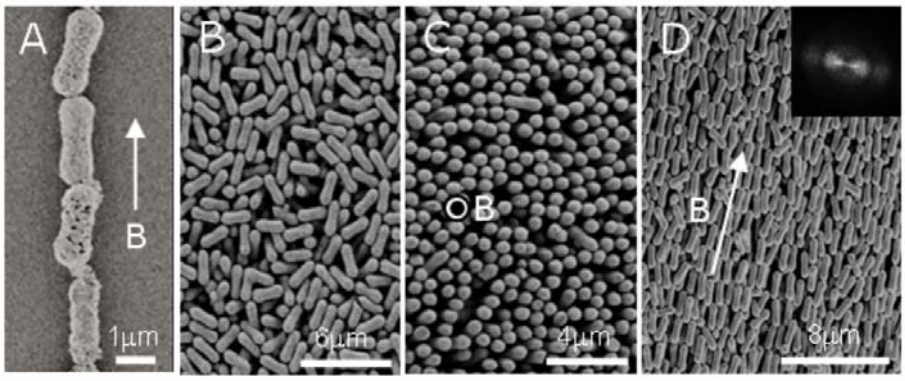

Figure 2.4. FE-SEM images of particle ordering under magnetic field-assisted assembly. a) Iron/magnetite colloids chain end-to-end due to dipolar attractions. b) A thin film of peanut-shaped, SiO_2-coated particles shows random orientations (control) when no field is applied. c) The same particles orient normal to the substrate plane when the applied field is pointed out-of-plane. d) Alignment of these particles in the substrate plane occurs when the external field is applied in the direction indicated by the white arrow. The inset shows a Fourier transform, indicating clear directional control of the peanut-shaped composite particles.

Upon drying, chains are also formed with particles oriented end-to-end (Figure 2.4a) due to dipolar attractions between the moments in each colloid. To exploit this property, droplets of the SiO_2-coated particles suspended in deionized water were placed onto a Si substrate and allowed to dry overnight under three conditions. In the first, no external field was applied; while in the second and third, a small neodynium bar magnet (850 Gauss) was positioned either perpendicular or parallel to the substrate. Figure 2.4b shows a FE-SEM image of the colloidal thin film formed in the first case, where peanut-shaped particles oriented randomly in all three dimensions. In contrast, the colloids are directed into nematic-like configurations either perpendicular or parallel to the substrate (Figure 2.4c-d) when an external field is applied in the corresponding direction. Some disorder in the particle orientations is evident, and can be attributed to thermal effects as well as surface tension drag during solvent evaporation. The preferred orientation of the SiO_2-coated particles in the substrate plane is further highlighted through the Fourier transform displayed as the inset of Figure 2.4d.

Although the hematite allows us to impart magnetic functionality, it may often be desirable to create hollow particles by eliminating the core component, for example in applications such as controlled release vehicles, microreactors, catalytic agents, and so forth. However, to prepare such particles from core-shell colloids introduces additional synthetic challenges. These range from finding the appropriate means of removing the core, to maintaining desirable material properties, colloidal stability, and structural integrity in the freestanding shells. We explored the preparation of hollow SiO_2, TiO_2, and ZnS through selective etching of the iron oxide core with hydrochloric acid. A representative TEM image for the silica case is shown in Figure 2.5a, which clearly illustrates robust, uniformly-coated, and hematite-free shells (77 nm). Because silica is chemically stable in HCl, the concentration and temperature during

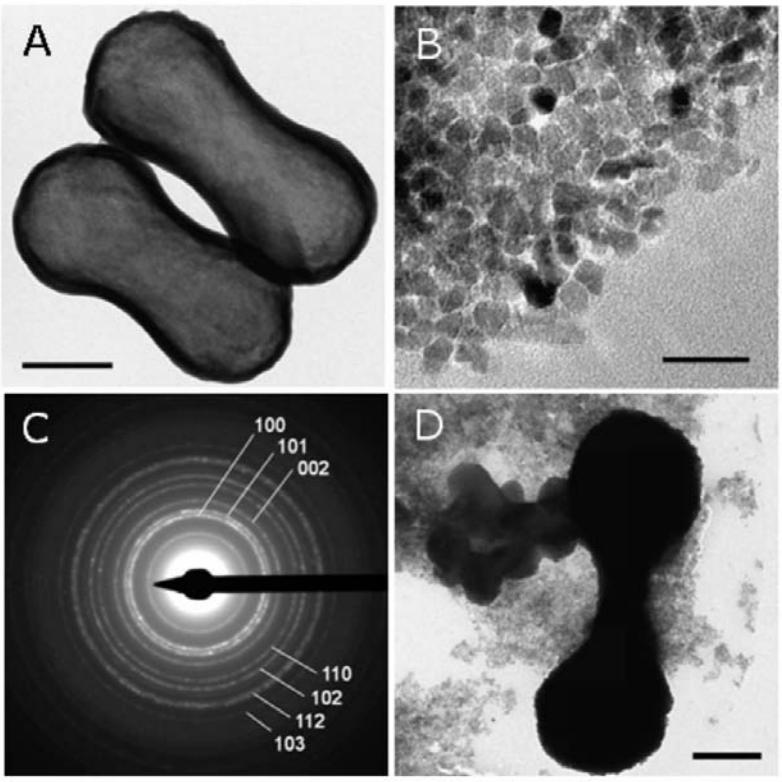

Figure 2.5. a) TEM image of robust, hollow SiO_2 shells (90min coating; shell thickness 77 nm) templated from peanut-shaped hematite core particles. Scale bar, 600 nm. b) The nanocrystals that remain in the α-Fe_2O_3-ZnS sample after dissolution in HCl. Scale bar, 40 nm. c) SAED pattern of b, which shows a faint inner ring corresponding to the (104) reflection of hematite, and successive specular rings indexed to the wurtzite polymorph of ZnS. d) TEM image of a partially-dissolved hematite particle in the α-Fe_2O_3-ZnS sample, suggesting anisotropic etching in the particle short axis direction. Scale bar, 400 nm.

dissolution did not require optimization. In fact, using a concentrated HCl (37%) at 45 ˚C for 2 hours was found to have no adverse effect on the SiO_2 shell integrity. To produce ZnS shells, dilute HCl (0.2 M) at 100 ˚C for 16 hours was used to avoid disintegrating the ZnS shell along with the hematite core. Despite the milder conditions however, TEM analysis revealed only clusters of small crystals (diameter ~15 nm) as seen in Figure 2.5b. Strikingly, selected area electron diffraction (SAED) yielded a specular ring pattern not consistent with the original sphalerite ZnS shell (Figure 2.5c). On the contrary, the faint inner ring appears to correspond to the hematite (104) reflection (from nanocrystals that are not yet entirely dissolved), while the successive spotted rings were indexed to the hexagonal wurtzite polymorph of ZnS. The exact formation mechanism of these crystals is unclear, although this scheme may be of interest as the sphalerite (cubic) $\rightarrow$ wurtzite (hexagonal) transformation is reported in ZnS nanoparticles only above T = 400 ˚C, or at a reduced temperature of T = 250 ˚C with 1 GPa of applied pressure.[22] In this wurtzite sample, a rare hematite core still in the early stages of dissolution was found under TEM inspection. Figure 2.5d shows its morphology and suggests that α-Fe_2O_3 colloids etch anisotropically. Specifically, the dissolution process appears to be preferred along the particle short axis direction, and is most dramatic at the narrow waist region of the peanut-shaped particles.

The same conditions (0.2 M HCl / 100 ˚C / 16 hours) were initially attempted on the α-Fe_2O_3/TiO_2 particles with limited success. TEM analysis (Figure 2.6a) revealed predominantly fragmented clusters, which withstood the chemical attack, amongst very few intact shells. To address this structural fragility, we calcined the composite particles at 400 ˚C for 3 hours to sinter and improve the mechanical properties of the metal oxide shell. During this process, the TiO_2 coating also crystallized into tetragonal anatase (JCPDS card no. 21-1272), as observed via XRD

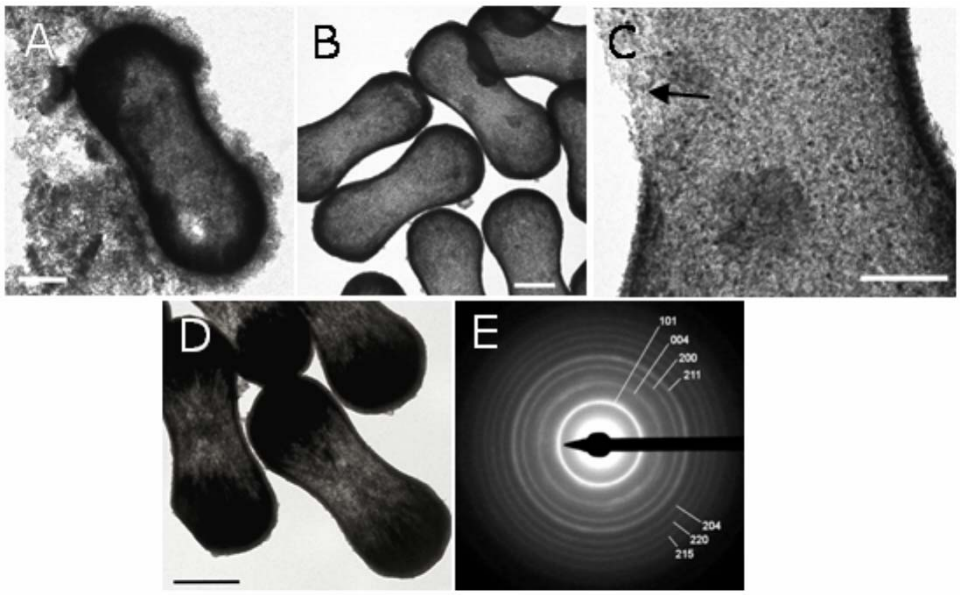

Figure 2.6. a) TEM image of amorphous TiO_2 peanut-shaped shells, which predominantly fractured after dissolution in HCl. Scale bar, 400 nm. b) Titania shells that were produced after annealing the core-shell particles prior to the chemical etch (0.2M HCl, 100 ^{o}C, 16 hours). Scale bar, 500 nm. c) Selected areas in b, which consisted of open holes (black arrow) in the TiO_2 shells. This phenomenon was most frequently observed in the particle waist region. Scale bar, 200 nm. d) TEM image of the particles from b etched in 0.2M HCl at 100 ^{o}C for only 10 hours. The uneven transparency in the bright-field image indicates further evidence of anisotropic etching in the hematite cores. Scale bar, 600 nm. e) SAED pattern of b, which is consistent with the anatase polymorph of titania.

(supporting information) by the appearance of the (100) reflection at 25.4˚. The diffracted intensities are relatively weak due to the small fraction of TiO_2 (~ 13%) in the core-shell samples. Under the same hydrochloric acid treatment, the anatase shells (48 nm) better maintained their peanut-shaped morphology (Figure 2.6b). We noted cases where a shell was inhomogeneously coated and formed surfaces with open holes. This effect was most pronounced at the waist region (Figure 2.6c), and may be due to large curvature differences in the core template, which tend to cause variations in the coating thickness. If the particles were treated with HCl for a reduced time of 10 hours, incomplete removal of the hematite core was found. A view of the partially-dissolved core-shell particles is shown in the bright-field TEM micrograph of Figure 2.6d. Anisotropic etching of α-Fe_2O_3 is again evident, as the colloids are consistently opaque (i.e., too thick to transmit the electron beam) on the far end of the lobes, but more fully etched and thus thinner in the waist region. SAED taken from completely hollow TiO_2 shells (Figure 2.6e) produced a pattern consistent with the XRD analysis for the tetragonal anatase phase of TiO_2.

An advantage of using titania in optical applications is that it exhibits a high refractive index. Here, we highlight this feature by trapping hollow anatase TiO_2 shells using holographic optical tweezers generated from a single laser source in an inverted microscope setup. Due to the particles' nonspherical shape, colloids were tilted vertically (with respect to the substrate plane) in the trap's field intensity gradient profile, and appeared sphere-like when imaged under bright-field, transmission mode. To constrain the peanut-shaped particles, TiO_2 shells were injected into a 2D confinement cell of height ~1 μm so that particles could only assume in-plane configurations. A series of optical micrograph time shots is illustrated in Figure 2.7. These images show five titania shells sequentially localized into a linear array by first trapping the particle, and then moving the trap and particle laterally together into the

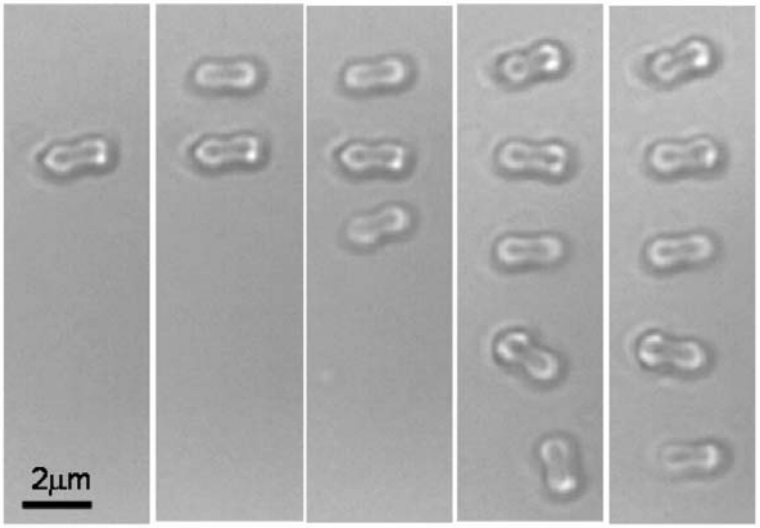

Figure 2.7. Optical microscope snapshots of five anatase TiO_2 shells being trapped into a linear array using holographic optical tweezers. Images were captured at t = 0, 8, 16, 31, and 32 seconds (from left to right) during the patterning process.

desired position. While confined to the traps each titania shell remained Brownian and did not stick to the glass substrate or wall. A video of the trapping process is included in the supporting information section.

In summary, particle systems having varied architectures (i.e., core-shell, hollow) and material properties (i.e., magnetic, optical) were produced to increase the scope and availability of functional nonspherical colloids. The peanut-shaped particles described here are expected to have application in diverse fields. For example, they could be used as tracers in the visualization of fluid dynamic flows i.e., using particle imaging velocimetry, or as magnetic micromixers in lab-on-a-chip devices. The dimer-like shape of the colloids may also be of value in ultimately building diamond-type colloidal crystals using a bottom-up approach. Finally, peanut-shaped particles may replace spherical probes in magnetic twisting cytometry (MTC) experiments. In this case, the ability to better visualize and control magnetic actuation should assist in the understanding of cell mechanotransduction.

Acknowledgements

We gratefully acknowledge funding of this work by the National Science Foundation Career Award No. DMR-0547976. The authors also thank Sharon Gerbode for assistance with the optical trapping experiments. This work was performed in part at facilities of the Cornell Center for Materials Research (NSF MRSEC, DMR-0520404).

Experimental

Iron Oxide Particle Synthesis: Peanut-shaped α-Fe_2O_3 particles were prepared by the gel-sol method as described by Sugimoto and co-workers[14]. In a typical synthesis, 45 mL of a NaOH solution (6.0 M) is added to 50 mL of a freshly prepared $FeCl_3$ solution (2.0 M, Mallinckrodt, pre-filtered using a 0.45 μm nitrocellulose membrane)

in a 100 mL Pyrex GL-45 bottle under vigorous magnetic stirring. Then, 5 mL of a Na_2SO_4 solution (0.6 M) is added and agitation is continued for an additional 10 minutes before the tightly sealed bottle is aged in an oven preheated at 100 ºC for 8 days. The particles were washed at least three times via centrifugation and resuspension in deionized water (18.2 MΩ-cm) before being recovered through filtration (0.45 μm nitrocellulose membrane) and dried overnight. To reduce α-Fe_2O_3 to iron/Fe_3O_4, the hematite samples were heated to 300 ºC under H_2 (flow rate, 10 ft^3/hour) for 3 hours.

Synthesis of Silica-, Titania- and Zinc Sulfide-coated Hematite: The silica-coated α-Fe_2O_3 particles were prepared by dispersing 1.0 g of the α-Fe_2O_3 powder in a mixture of 84 mL 2-propanol ($(CH_3)_2CHOH$), 12 mL NH_4OH (27%) and 4 mL deionized H_2O (18.2 MΩ-cm) in a 100 mL round-bottomed flask immersed in a constant temperature bath of 30 ºC. To prevent agglomeration and sedimentation during the coating procedure, a sonicator probe operating at 12-14 W was immersed into the mixture and applied for 90 minutes to 4 hours immediately after the addition of 0.3 mL tetraethylorthosilicate ($Si(OC_2H_5)_4$, Aldrich, 98%). The titania-coated α-Fe_2O_3 particles were prepared by dispersing 0.3 g of the α-Fe_2O_3 powder in a mixture of 20 mL ethanol, 0.15 ml NaCl solution (5 mM), and 0.125 mL of the titanium tetraisopropoxide precursor ($Ti(CH_3CHOCH_3)_4$, Aldrich, 97%). The mixture was sealed in a vial and kept in a 90 ºC oven for 45 minutes. The ZnS-coated particles were prepared by dispersing 0.2 g of the α-Fe_2O_3 powder in a mixture of 300 mg zinc acetate ($Zn(CH_3COO)_2$, Aldrich) and 100 mg thioacetamide (CH_3CSNH_2, Aldrich, 99%) dissolved in 100 mL of deionized H_2O (18.2 MΩ-cm). The sonication (12 W) time was 2 hours without temperature control. At the end of each synthesis, particles were isolated and collected by repeated centrifugation and resuspension in deionized

water (pH 7). As before, samples were reduced by heating to 300 ºC under H_2 (flow rate, 10 ft^3/hour) for 3 hours.

Assembly of Peanut-shaped Colloids using a Magnetic Field: The assembly of the peanut-shaped colloids was achieved via slow drying under ambient conditions in the presence of an external magnetic field. A droplet of the particle suspension (10 mg/mL) was deposited on a silicon wafer pre-cleaned with deionized water and ethanol. To orient the particles, a small neodynium bar magnet (~850 Gauss) was placed adjacent to the droplet either with the magnetic field oriented perpendicular or parallel to the substrate. The droplet was left to dry overnight and the resulting structures were characterized via electron microscopy.

Optical Trapping of Hollow TiO_2 Shells: Hollow anatase shells were trapped using an inverted microscope setup with a Zeiss Plan-apochromat objective lens (100x oil immersion, 1.4 NA) and a 800 mW laser operating at 1064 nm. A spatial light modulator (Boulder Nonlinear Systems) was employed to separate the beam into multiple traps. To confine the particles into a monolayer, a wedge-shaped confinement cell was used as described previously.[18]

Materials Characterization: Samples were characterized using field emission scanning electron microscopy (FE-SEM; Zeiss-1550), transmission electron microscopy (TEM; FEI Tecnai T-12, 120 kV), X-ray powder diffraction (Scintag, PAD X, Cu K_α λ=1.5406 Å), energy dispersive spectroscopy (EDS; JEOL 8900 EPMA microprobe), and vibrating sample magnetometry (VSM; Lakeshore Cryogenic 7300).

APPENDIX

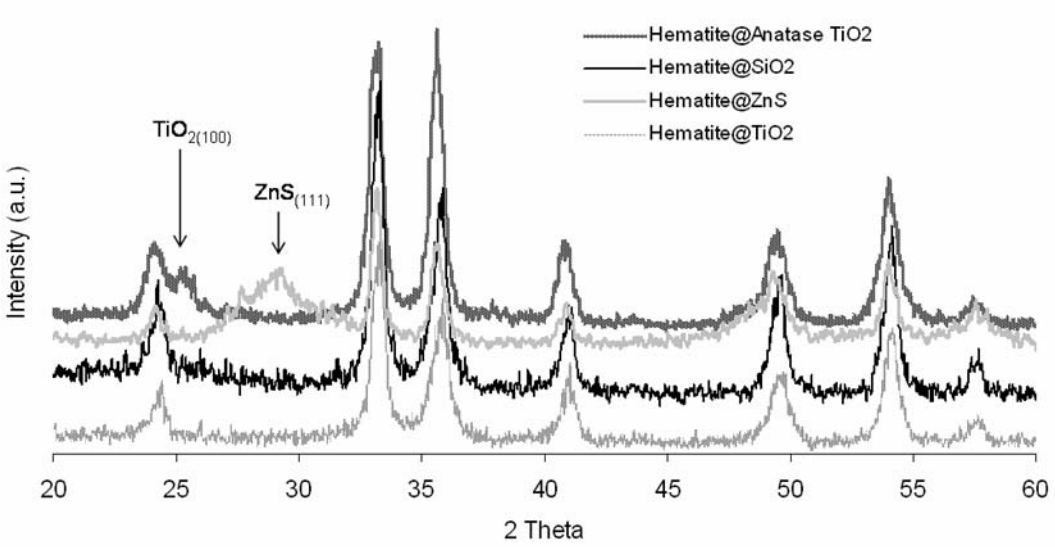

Figure 2.S1. XRD pattern for various hematite core-shell samples (from top to bottom): α-Fe_2O_3-TiO_2 (anatase), α-Fe_2O_3-ZnS, α-Fe_2O_3-SiO_2, and α-Fe_2O_3-TiO_2 (amorphous).

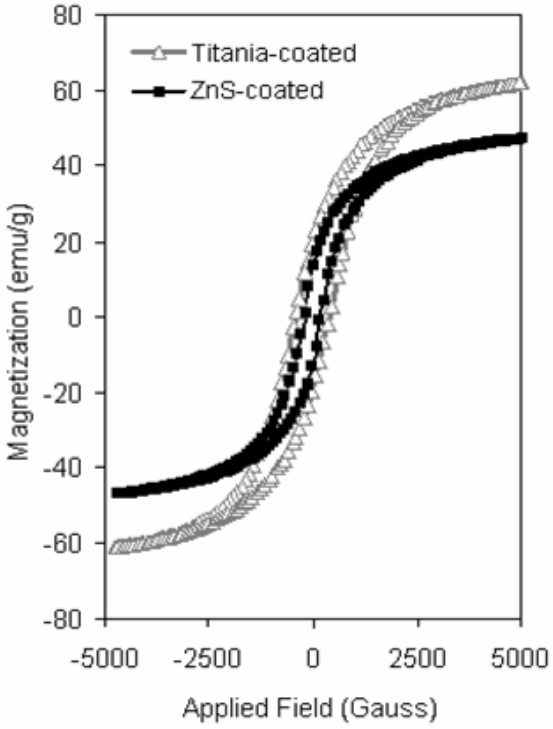

Figure 2.S2. VSM hysteresis loops for titania- and zinc sulfide-coated hematite particles after reduction (measured at room temperature).

REFERENCES

1. Y. Xia, B. Gates, Y. Yin and Y. Lu. *Advanced Materials*, **12**, 693 (2000).

2. F. Caruso. Nanoengineering of particle surfaces. *Advanced Materials*, **13**, 11 (2001).

3. V. Salgueiriño-Maceira and M. A. Correa-Duarte. *Advanced Materials*, **19**, 4131 (2007).

4. X. Gao, Y. Cui, R. M. levenson, L. W. K. Chung and S. Nie. *Nature Biotechnology*, **22**, 969 (2004).

5. D. Talapin, A. L. Rogach, A. Kornowski, M. Haase and H. Weller. *Nano Letters*, **1**, 207 (2001).

6. Y. Lu, Y. Yin and Y. N. Xia. *Advanced Materials*, **13**, 271 (2001).

7. X. W. Lou and L. A. Archer. *Advanced Materials*, **20**, 1853 (2008).

8. L. Y. Hao, C. L. Zhu, W. Q. Jiang, C. N. Chen, Y. Hu and Z. Y. Chen. *Journal of Materials Chemistry*, **14**, 2929 (2004).

9. X. W. Lou, C. Yuan and L. A. Archer. *Advanced Materials*, **19**, 3328 (2007).

10. M. Ohmori and E. Matijevic. *Journal of Colloid and Interface Science*, **160**, 288 (1993).

11. Y. Lu, Y. Yin and Y. N. Xia. *Advanced Materials*, **13**, 415 (2001).

12. K. M. Ho, C. T. Chan and C. M. Soukoulis. *Physical Review Letters*, **65**, 3152 (1990).

13. L. Au, D. Zheng, F. Zhou, Z.Y. Li, X. Li and Y. N. Xia. *ACS Nano*, **2**, 1645 (2008).

14. S. Sacanna, L. Rossi, B. W. M. Kuipers and A. P. Philipse. *Langmuir*, **22**, 1822 (2006).

15. T. Sugimoto, M. M. Khan and A. Muramatsu. *Colloids and Surfaces A-Physicochemical and Engineering Aspects*, **70**, 167 (1993).

16. Q. Liu and K. Osseo-Asare. Journal of Colloid and Interface *Science*, **231**, 401 (2000).

17. S. Liu, J. Yu, B. Cheng, L. Zhao and Q. Zhang. *Journal of Crystal Growth*, **279**, 461 (2005).

18. S. H. Lee, S. J. Gerbode, B. S. John, A. K. Wolfgang, F. A. Escobedo, I. Cohen and C. M. Liddell. *Journal of Materials Chemistry*, **18**, 4912 (2008).

19. H. Itoh and T. Sugimoto, *Journal of Colloid and Interface Scienc*e, **265**, 283 (2003).

20. A. H. Morrish. *Canted antiferromagnetism: Hematite* (World Scientific Publishing Company, 1994).

21. F. E. Luborsky and T. O. Paine. *Journal of Applied Physics*, **31**, S68 (1960).

22. C. Yang, Y. Liu, H. Sun, D. Guo, X. Li, W. Li, B. Liu and X. Zhang. *Nanotechnology*, **19**, 095704 (2008).

CHAPTER 3

SYNTHESIS AND ASSEMBLY OF NONSPHERICAL HOLLOW SILICA COLLOIDS UNDER CONFINEMENT*

Colloidal self-assembly has long been cited as a means to create periodic materials for photonic, optoelectronic, solar cell, and sensing applications. The technique is attractive because it holds promise for the simple microfabrication of low-cost, large-scale devices. Nevertheless, structures that are accessible with spherical particles have generally been restricted to the rather common hexagonal close-packed or face-centered cubic forms, except in the case of bidisperse systems (i.e., size and charge).[1,2] The lack of diversity is a result of isotropic interactions in spherical particles, which fail to capture the selective functionalities and geometries required to encode the ordering of more elaborate assemblies. In contrast are sophisticated structures such as icosahedral virus capsids and herringbone pentacene thin films, which use protein sub-units or small molecules as their structural motifs. These architectures inspire a strategy to increase complexity in traditional colloids by introducing symmetry-breaking features in the particle shape or interparticle potential. Essential to this idea is the ability to impart specific assembly instructions to the colloidal building blocks so that materials with enhanced functional properties can be made.

Approaches to induce directional interactions include using shape-selective depletion forces, which in disk-shaped colloids led to the formation of columnar

---

* Originally Published as: Stephanie H. Lee, Sharon J. Gerbode, Bettina S. John, Angie K. Wolfgang, Fernando A. Escobedo, Itai Cohen and Chekesha M. Liddell. "Synthesis and assembly of nonspherical hollow silica colloids under confinement", *J Mater Chem*, **18**, 4912 (2008). *Reprinted by permission of The Royal Society of Chemistry*, http://www.rsc.org/Publishing/Journals/JM/article.asp?doi=b812406j.

structures,[3] or dipolar forces, which in spherical particles led to the formation of body-centered tetragonal assemblies.[4] Intricate building blocks consisting of spherical particles with directional patches have also been synthesized recently.[5] Simulations predict that under the right conditions these particles can form a diamond structure,[6] one of the best candidates for a complete photonic bandgap material. Other theoretical predictions have indicated that a rich number of phases can be realized through the self-assembly of nonspherical particles. For instance, heteronuclear dimers were predicted to condense into a methyl chloride-like structure, given a sufficient electric dipole moment per particle.[7] Hard spherocylinders of different aspect ratios also ordered into stable states that included orientationally-ordered solids with AAA or ABC stacking and a plastic crystal phase.[8] These simulations illustrate the potential to produce colloidal assembly analogues by design, especially when viewed in light of recent progress in colloidal synthesis techniques, which yield particles of exotic shape, functionality, and high monodispersity.[9-14] In spite of these advances, relatively few well-defined structures have been made thus far from complex-shaped colloids.[15,16]

The present work highlights the synthesis of peanut-shaped particles with hard dimer-like interactions and demonstrates their assembly into ordered structures under confinement. The particles were prepared through a multi-step templating process that produced hollow, fluorescent silica shells amenable to direct visualization with a confocal microscope. To synthesize the core hematite particles (α-Fe_2O_3), a condensed ferric hydroxide gel was first aged under hydrothermal conditions (Figure 3.1a).[17] A rhodamine-functionalized silica shell was then grown onto the hematite surface using modified sol-gel chemistry.[18] This protocol produced 95% pure dimer particles with final dimensions of 2.82 μm $\times$ 1.36 μm, and a coefficient of variation of 4.7%. The thickness of the shells ranged between 20-150 nm and was tuned via suitable selection of the silica precursor concentration and feed times. Since hematite has a high index of

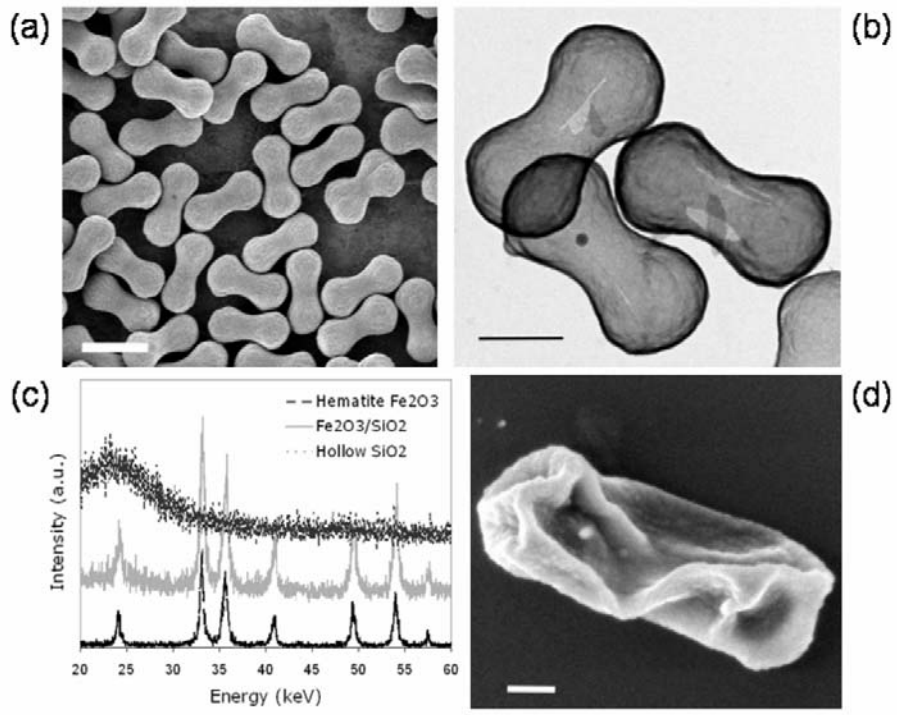

Figure 3.1. Fluorescent silica particles. a) FE-SEM image of monodispersed hematite colloids from which hollow particles were templated. Scale bar, 2 microns. b) TEM bright-field micrograph of intact silica shells (thickness, 65 nm). Scale bar, 900 nm. c) XRD pattern of hematite particles (bottom, black), hematite-silica core-shell particles (middle, light gray), and hollow silica shells (top, dark gray). The bottom two show peaks corresponding to crystalline hematite (JCPDS card no. 33-0664) while the top exhibits only an amorphous signature indicative of complete etching. d) Collapsed particle (thickness, 28 nm), illustrating a typical morphology below the critical thickness, t_c. Scale bar, 300 nm.

refraction that hinders confocal imaging due to scattering, and a weak magnetization that alters the assembly process, the core was sacrificed through selective etching using concentrated hydrochloric acid (Figure 3.1b). Complete removal of the hematite was confirmed by XRD (Figure 3.1c).

Peanut-shaped shells were found to be structurally stable only when the thinnest coating regions passed a critical shell thickness of 46 ± 10 nm. Below this thickness, hollow dimers crumpled without fracture and lost their intended shape (Figure 3.1d). A high-magnification FE-SEM micrograph is shown in the inset (Figure 3.1d) to illustrate the details of the collapsed morphology. Increasing the silica precursor concentration led to thicker shells, though coatings were limited to ~65 nm depositions in a single step to prevent the undesirable nucleation of smaller, secondary silica particles. The particles were sterically-stabilized and suspended in an aqueous solution which yielded nearly hard body interactions. If the cores were left intact however, dipolar attractions due to the antiferromagnetic hematite led to chains and nematic-like structures. This phenomenon will be discussed elsewhere.

Here, the ordering of a dense monolayer of dimers was investigated for hollow particles confined in a wedge geometry cell (Figure 3.2a). Particle area fraction was controlled by gently tilting the cell so that the dimers slowly sedimented into the region of interest. Before imaging, the confinement cell was laid flat to allow for equilibration over the entire field of view. The spontaneous organization of the colloids at high area fraction is shown in the confocal micrograph of Figure 3.2b. Although the positions of the particle centers are aperiodic, an image captured at a focal plane that grazes only the particle tips reveals triangular ordering in the lobes (Figure 3.2c). This symmetry is quantified by the form of the lobe pair correlation function, g(r), taken over an area of 4800 μm^2 (Figure 3.3a). As demonstrated by the trimodal distribution in Figure 3.3b, peanut-shaped colloids oriented with equal

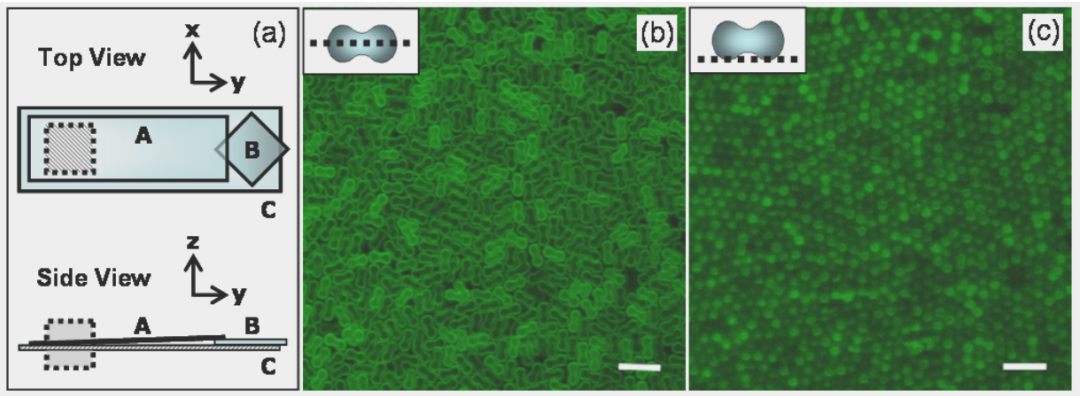

Figure 3.2. Confocal microscopy of dense monolayers of peanut-shaped particles. a) Schematic of wedge-shaped confinement cell used to constrain the nonspherical dimer colloids. Part A represents a long coverslip, B a spacer coverslip, and C the microscope slide substrate. The hatched area indicates a region where the z-height is roughly 1.5 μm. b) Confocal image of a dense monolayer of colloids taken across the equatorial plane (inset, schematic view). Scale bar, 5 microns. c) Triangular ordering of the lobes is revealed when an image is captured at a focal plane that just grazes the particle lobes (inset, schematic). Scale bar, 5 microns.

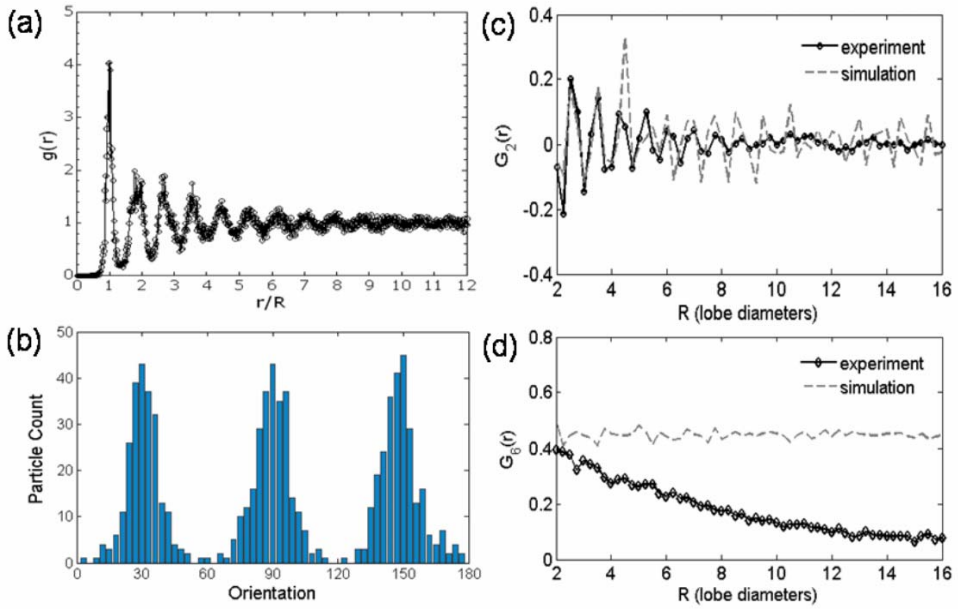

Figure 3.3. Structural characterization. a) Lobe radial distribution function, g(r). b) Histogram of particle orientations taken from various crystallites. The first peak measured from each grain was shifted to $\theta = 30^{o}$ to illustrate the trimodal distribution clearly. c) The dimer orientation correlation function, $G_2(r)$, oscillates about zero and indicates a low degree of alignment in the dimer molecular axes. d) The orientation correlation function, $G_6(r)$, shows non-zero but decreasing long-range order, indicating that particle orientations are close to multiples of $\pi/3$.

probability along the three crystalline axes defined by the lobes. In addition, because the interparticle angles occur predominantly at intervals of θ/3, they can be well characterized by the orientation correlation function:

$$G_6(r) = \left\langle \sum_{i \le i < j \le N} \cos(6\Delta\theta_{ij}) \cdot \delta(r_{ij} - r) \right\rangle$$

where $\Delta\theta_{ij}$ is the difference in orientation between the i^{th} and j^{th} particle, and r_{ij} is the distance between their centers-of-mass. The function $G_6(r)$ gives spatial information on the dimer orientations and expresses their degree of ordering to $\Delta\theta_{ij}$ values of $n\pi/3$, where n is an integer. Given perfect lobe positional order and dimer orientations, $G_6(r)$ should equal unity. In the experimental system (Figure 3.3c), $G_6(r)$ exhibits lower values due to the angular spread in $\Delta\theta_{ij}$ (Figure 3.2b). It also displays a decaying long-range orientational order in the dimer axes, which may be suggestive of crystalline defects or grain boundaries.

The observed structure is reminiscent of the degenerate crystal (DC),[19] which has thus far been seen only in MC simulations of dimers with aspect ratio ≤ 2. As with our colloidal particles, in the simulated DCs, dimer lobes tile a triangular lattice while particle orientations populate one of three crystalline directions. Such a phase exhibits strong configurational degeneracy, and was determined numerically to be the thermodynamically-stable phase.[20] An additional feature characterizing DCs is that the dimer centers irregularly decorate a kagomé lattice so that exactly one site is occupied in each unit hexagon (Figure 3.4a). Although the particles in the current study are elongated with aspect ratio 2.074, rather than shortened as in the MC simulations, the particle centers were found to satisfy this kagomé requirement (Figure 3.4b).

A distinct difference between the simulated single-grain DCs and the observed structures was that the latter always contained many crystallites with an average

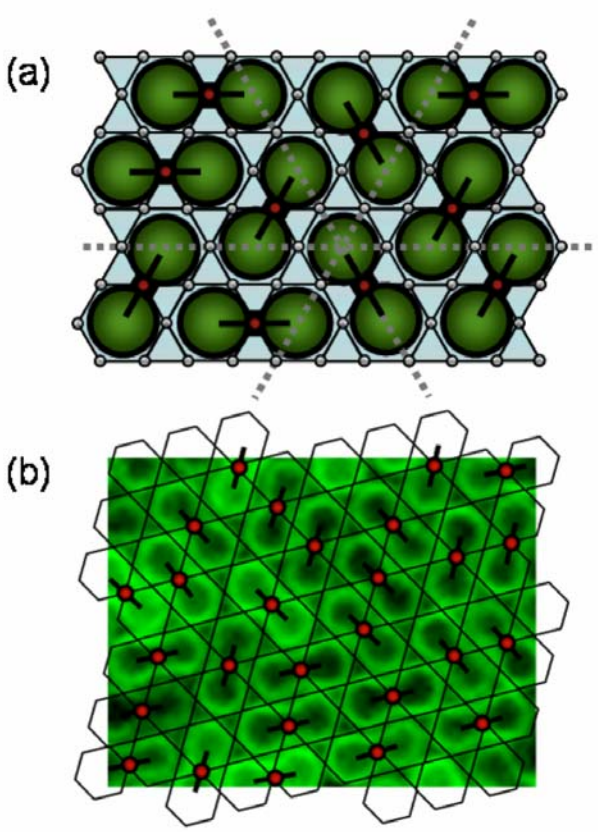

Figure 3.4. Kagomé construction of the Degenerate Crystal (DC). a) A schematic showing the structure of the DCs observed in prior simulations.[20] Red dots represent the particle centers-of-mass, white circles show the kagomé lattice sites, and dashed grey lines indicate the three crystalline axes (after Ref 19). b) Kagomé construction applied to the experimental data with peanut-shaped colloids. The overlaid kagomé net is a guide for the eye.

dimension of 10 ± 1 lobe diameters. This small grain size is reflected in the lobe pair correlation function, whose peaks decay beyond this length scale (Figure 3.3a). Figure 3.5a highlights the defect distribution in a typical sample using a Voronoi reconstruction, in which every particle lobe is colored according to its coordination number. This schematic reveals that while some defects are isolated, many coalesce into string-like grain boundaries separating DC crystallites of different orientations. The mean fraction of defects is 15%, and of those, 61% are located on the grain boundaries. While both types of defects were mobile, their total numbers remained nearly constant over a time scale of weeks. The observation of defect mobility in the experimental DC is in stark contrast to defects in crystalline monolayers of hard spheres with comparable particle size and area fractions, which anneal over a time scale of hours.

The importance of defect mobility lies in its crucial role in determining many material properties ranging from yield and plastic flow to work hardening and fatigue. In crystals of spheres the motion of defects is achieved through simple particle rearrangements. In the dimer system however, each lobe is permanently attached to one of its neighbors, and thus a rearrangement necessitates not only a translational, but also an orientational change. To illustrate the significance of this lobe pairing on defect annealing, and consequently on defect fractions, Monte Carlo (MC) simulations of crystalline monolayers of spheres and dimers formed under compression were compared. Ideal monodisperse particles were modeled in an isothermal ensemble starting from a disordered state at low density. The system was then compressed by incrementally increasing the pressure until it crystallized (Figure 3.5b-c). In these simulations, compression rates were varied by changing the number of MC cycles used for equilibration at each pressure. Figure 3.5d illustrates that crystals of dimers had a higher fraction of defects than crystals of spheres at all compression rates.

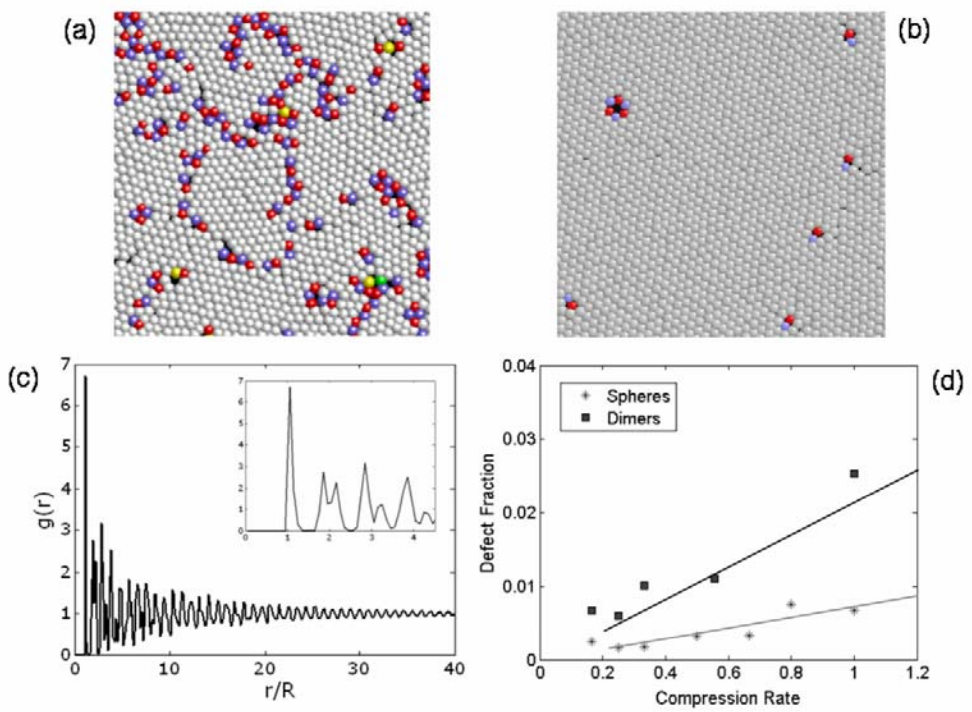

Figure 3.5. Defects and Monte Carlo simulations. a) Voronoi reconstruction for the experimental data, which shows N = 2394 particle lobes color-coded by their coordination number. Defects, consisting of lobes with a coordination number other than six, were highlighted with non-white colors. b) Voronoi reconstruction from MC simulations at a compression rate of 0.17. A magnified region of the sample area (N = 7200 lobes) is shown for clarity. c) Lobe pair correlation function associated with the simulation set from b. Inset, magnified view of the first few peaks. d) Comparison of the defect fraction in crystals made of peanut-shaped dimers (black squares) versus spherical particles (grey asterisks) at various compression rates. Trend lines were added to guide the eye.

Furthermore, this effect is more pronounced at higher compression rates, where the fraction of defects increases for dimers but remains nearly zero for spheres. These MC simulations, in conjunction with the experiments, suggest that defect dynamics in DCs may be considerably more constrained than those in crystals of spheres. Future investigations should help to clarify the differences in defect transport that lead to the observed disparity in annealing times. In addition, it would be of interest to probe whether DCs have long-range orientational order, but short-range translational order, as is characteristic of a hexatic phase. Such ordering is challenging to identify however, particularly when dealing with the case of hard-sphere or polycrystalline systems.

The present report illustrates that proper selection and synthetic control of colloidal building blocks can open opportunities for the self-assembly of materials with novel structures, as exemplified by the observed DCs. Further studies, such as transition path sampling simulations and nucleation and growth experiments, should help to elucidate the mechanisms of the isotropic to DC phase transition. It may also be possible to design new assemblies of these particles by introducing further interactions with templated substrates. Observations of colloidal assembly on such surfaces may provide intuition for atomic scale processes, such as the physisorption and phase transitions of diatomic molecules on graphite/Au/Ag films.[21] It has been shown that pairing constraints in DCs lead to interesting mechanical properties such as a low Poisson's ratio.[22] If 3D versions of these phases exhibit a similarly low Poisson's ratio, they could be valuable as materials for the manufacture of piezoelectric composites, used commonly in low-frequency actuators of sonar arrays and seismic monitors.[23] Most importantly, our studies of these simple anisotropic particles hint at the diversity of assemblies that can be constructed using nonspherical colloids. As such, it represents a positive step towards achieving molecular mimicry,

whereby self-organization of systems with novel properties is driven by codes embedded within the constituent building blocks.

Acknowledgements

We gratefully acknowledge funding of this work by the National Science Foundation (Career Award No. DMR-0547976, DMR-0606040, DMR-0553719) and the American Chemical Society PRF Grant #45525-AC7. Additionally, this work was performed in part at facilities of the Cornell Center for Materials Research (NSF MRSEC, DMR-0520404).

Experimental

Particle Synthesis

Core peanut-shaped α-Fe_2O_3 particles were prepared by a gel-sol method as described previously[23]. In a typical synthesis, 50 mL of $FeCl_3$ (2.0 M) was mixed with 45 mL of NaOH (6.0 M) and 5 mL of Na_2SO_4 (0.6 M) and aged in a preheated oven (100 ºC) for 8 days. A layer of rhodamine isothiocyanate (RITC)-modified silica was then coated onto the α-Fe_2O_3 cores via a modified Stöber synthesis[24] conducted under sonochemical conditions (probe power 14 W, 30 ºC). To make shells approximately 65 nm thick, the reaction mixture comprised: 0.4% (w/v) hematite powder, 0.25% (v/v) rhodamine dye solution, 7.1 M deionized water, 0.92 M ammonia, and 17.4 mM tetraorthoethylsilicate (TEOS) added batch-wise to isopropyl alcohol medium. Hollow silica shells were made by selectively removing the core with concentrated hydrochloric acid (18%) after surface modification with polyvinylpyrrolidone (PVP, 30k MW). Before use, colloids were titrated to neutral pH and washed via repeated centrifugation and decanting before being re-dispersed into deionized water.

Sample Preparation

The wedge-shaped confinement cell was assembled by fixing three sides of a 22 x 50 mm glass coverslip (VWR, No. 1½) to a large microscope slide and propping the last side up with a 22 x 22 mm spacer coverslip. Three sides of the coverslip were sealed with Norland UV optical glue, cured overnight, and reinforced with 5-minute epoxy. To load the particles, a dilute peanut-shaped colloidal dispersion was injected into the cell at the open end via a micropipette tip and was sealed with epoxy. The wedge cell was titled 10-60 degrees from horizontal to control the area fraction of particles within the region of interest by allowing the colloids to sediment. After sufficient densification, the cell was laid flat to re-establish equilibrium. Particles were visualized directly using a confocal microscope.

System Characterization

SEM images were collected using an LEO 1550 field emission scanning electron microscope (FE-SEM) at 0.5-3 kV. TEM micrographs were captured with an FEI Tecnai T12 Spirit Twin transmission electron microscope at an operating voltage of 120 kV. To determine the SiO_2 shell thickness, values were measured from 50 points on hollow shells using TEM images, with the uncertainty given by the standard deviation. XRD spectra were obtained using Cu Kα radiation on a Scintag θ-θ diffractometer equipped with an intrinsic germanium detector. For confocal data, a Zeiss LSM 5 LIVE inverted laser scanning confocal microscope with an excitation wavelength of 532 nm was used.

Monte Carlo (MC) Simulations

In the Monte Carlo (MC) simulations, monolayers of peanut-shaped or spherical particles were compressed until they crystallized. The peanut-shaped dimers (N =

3600) were modeled as two spheres whose centers were located a distance of 1.075 particle diameters apart. The samples were kept at isothermal conditions throughout the simulations. Compression was achieved by increasing the pressure in steps and allowing for equilibration at each step using translation and rotation of randomly chosen dimers, with an acceptance rate based on the Metropolis criteria. The compression rate was initially defined as the ratio of the Gibbs free energy difference, ΔG, between initial and final pressures P_1 and P_2, to the total number of MC cycles in millions of cycles. The value of ΔG was chosen such that it was always the same and thus provided the same thermodynamic driving force toward compression for the dimer and spherical particles, even though crystallization for the two systems occur at different area fractions. Because ΔG is constant, we then simply redefined the compression rate as the reciprocal of the millions of MC cycles used to go from P1 and P2. ΔG was found from $\Delta G = \int_{P_1}^{P_2} AdP$, where A is the total surface area of the system, and P1 and P2 were chosen such that: (i) P1(P2) was well inside the isotropic(crystal) branch of the equation of state, and (ii) ΔG between P1 and the isotropic-crystal transition pressure P*, and ΔG between P* and P2 were the same across both the dimer and sphere systems. The integrations were evaluated based on the equilibrium equation of state data. For the spheres: P1 = 5 (surface coverage, SC = 0.601) and P2 = 14.8 (equilibrium SC ~0.785); For the dimers: P1 = 3.4 (SC ~0.624) and P2 = 13.0 (equilibrium SC = 0.843). The compression rate was maintained at a low enough value to allow the systems to approach the final equilibrium surface coverage and crystallize. Since crystals of spheres always formed single grains, simulation results were also restricted to those that formed single DC grains in order to compare the two systems on an equal basis.

REFERENCES

1. E. V. Shevchenko, D. V. Talapin, N. A. Kotov, S. O'Brien and C. B. Murray. *Nature*, **439**, 55 (2006).

2. M. E. Leunissen, C. G. Christova, A. P. Hynninen, C. P. Royall, A. I. Campbell, A. Imhof, M. Dijkstra, R. Van Roij and A. van Blaaderen. *Nature*, **437**, 235-240 (2005).

3. S. Badaire, C. Cottin-Bizonne, J. W. Woody, A. Yang and A. D. Stroock. *Journal of the American Chemical Society,* **129**, 40 (2007).

4. A. Yethiraj and A. van Blaaderen. *Nature*, **421**, 513 (2003).

5. Y. S. Cho. G. R. Yi, S. H. Kim, S. J. Jeon, M. T. Elsesser, H. K. Yu, S. M. Yang and D. J. Pine. *Chemistry of Materials*, **19**, 3183 (2007).

6. Z. L. Zhang, A. S. Keys, T. Chen and S. C. Glotzer. *Langmuir*, **21**, 11547 (2005).

7. S. C. Gay, P. D. Beale and J. C. Rainwater. *Journal of Chemical Physics*, **109**, 6820 (1998).

8. P. Bolhuis and D. Frenkel. *Journal of Chemical Physics*, **106**, 666 (1997).

9. J. W. Kim, R. J. Larsen and D. A. Weitz. *Journal of the American Chemical Society*, **128**, 14374-14377 (2006).

10. D. Dendukuri, D. C. Pregibon, J. Collins, T. A. Hatton and P. S. Doyle. *Nature Materials*, **5**, 365 (2006).

11. Y. S. Cho, G. R. Yi, J. M. Lim, S. H. Kim, V. N. Manoharan, D. J. Pine and S. M. Yang. *Journal of the American Chemical Society*, **127**, 15968 (2005).

12. P. M. Johnson, C. M. van Kats and A. van Blaaderen. *Langmuir*, **21**, 11510 (2005).

13. V. N. Manoharan, M. T. Elsesser and D. J. Pine. *Science*, **301**, 483 (2003).

14. C. M. Liddell and C. J. Summers. *Advanced Materials*, **15**, 1715 (2003).

15. E. B. Mockand C. F. Zukoski. *Langmuir*, **23**, 8760 (2007).

16. I. D. Hosein and C. M. Liddell. *Langmuir*, **23**, 10479 (2007).

17. T. Sugimoto, M. M. Khan and A. Muramatsu. *Colloids and Surfaces A-Physicochemical and Engineering Aspects*, **70**, 167 (1993).

18. A. van Blaaderen and A. Vrij. *Langmuir*, **8**, 2921 (1992).

19. K. W. Wojciechowski, D. Frenkel and A. C. Branka. *Physical Review Letters*, **66**, 3168 (1991).

20. K. W. Wojciechowski. *Physical Review B*, **46**, 26 (1992).

21. M. F. Toney, R. D. Diehl and S. C. Fain. *Physical Review B*, **27**, 6413 (1983).

22. K. V. Tretiakov and K. W. Wojciechowski. *Journal of Non-Crystalline Solids*, **352**, 4221 (2006).

23. A. Perry, C. R. Bowen and S. W. Mahon. *Scripta Materiali*a, **41**, 1001 (1999).

CHAPTER 4

ANISOTROPIC MAGNETIC COLLOIDS: A STRATEGY TO FORM COMPLEX STRUCTURES USING NONSPHERICAL BUILDING BLOCKS*

Microscopic magnetic particles dispersed in a solvent – or dipolar colloidal fluids – commonly assemble into chains due to a directional attractive interparticle potential. These chained structures can impart optical anisotropy (i.e., birefringence) to dipolar fluids,[1] and have been demonstrated as effective matrix materials in the rapid separation of DNA using microfluidic electrophoresis.[2] In the special case of magnetorheological (MR) systems, which require external fields to induce dipoles in polarizable colloids, an abrupt microstructural transition from isolated (unpolarized) particles into oriented chains can produce dramatic changes in the viscous behavior.[3] This responsive property makes MR fluids attractive as field-controllable damping fluids in hydraulic valves, shock absorbers, and brakes, etc.[4]

Dipolar fluids also display interesting ordering phenomena beyond the 1D case. For instance, nickel-coated glass microspheres were shown to pack onto square, oblique, triangular, and even quasi-crystalline lattices with five-fold symmetry in 2D.[5a] Binary particle mixtures assembled into "flower"-like aggregates and superlattices in a planar configuration.[5b,c] In 3D, dipolar fluids were predicted to form rich mesophases as a function of the dipole moment strength, particle volume fraction,

* To be Published as: Stephanie H. Lee and Chekesha M. Liddell. "Anisotropic magnetic colloids: a strategy to form complex structures using nonspherical building blocks", *Small*, in press (2009).

and the relative 'hard' or 'soft' nature of the colloidal interactions.[6] Examples include the body-centered-tetragonal (bct) and body-centered-orthorhombic (bco) crystals, along with a broad fluid-bct co-existence phase. Yethiraj and van Blaaderen[7] demonstrated these phases experimentally using a system with tunable long-range repulsive (isotropic) and dipolar (anisotropic) interactions. Such a model system is useful for the exploration of uncommon colloidal structures and for the elucidation of phase phenomena, including the field-induced solid–solid transformations between face-centered-cubic (fcc) and bct crystals.

A recent trend in colloid science suggests an emerging theme of applying complex particles as structural motifs for an ever increasing array of synthetic materials. Significant progress in the fabrication of submicron- and micron-sized colloids in the past few years has yielded particles with various nonspherical shape,[8] 'patchy' functionality,[8a,9] and anisotropic properties ranging from amphiphilicity[10] and polarizability,[11] to magnetic anisotropy.[12] An important consideration in the pursuit of self-assembly strategies using such building blocks is to ensure that interactions are well-controlled. Thus, selectivity in 'bonds' and weak interactions are often more desirable for equilibrium structures, as this allows systems to evolve toward the target structure in a reversible fashion. With regards to nonspherical colloids, in particular, a major challenge remains in the limited ability to control the orientation, localization, and registry of the particles.

Here, we report the synthesis and microstructure of peanut-shaped colloids with a permanent transverse magnetic dipole, and describe their organization into complex 1D and 2D structures. This work illustrates, in particular, the effect that hierarchical structure and colloidal properties have on the resulting self-assembly behavior. As with spherical dipolar fluids, these colloids aggregate into chains oriented along an applied magnetic field. Features that distinguish this system are: (1)

the high degree of orientational alignment in each particle, (2) a striking selectivity in the side-by-side interaction, and (3) shape complementarity in the peanut-type morphology, which allows colloids to close-pack and form kinked zigzag chains when confined to a planar geometry. We approximate the free energy of a single chain bond using a simple linear aggregation model, and show qualitative evidence for reversibility in this system. Significantly, the zigzag aggregates coarsen at high surface fractions to form 2D crystallites separated by voids. These crystallites have characteristics of molecular crystal-type phases[13] and display the oblique symmetry of the *p2* plane group.

Figure 4.1a shows a field emission scanning electron micrograph (FE-SEM) of the peanut-shaped hematite (α-Fe_2O_3) colloids synthesized by aging a condensed $Fe(OH)_3$ gel in the presence of a shape modifier, Na_2SO_4.[14] Each particle (length = 2.60 μm; lobe diameter = 1.18 μm) is composed of many acicular crystallites, all roughly oriented along the particle's major axis, but with some radial splay particularly in the two constituent lobes. The microstructure can be easily seen in transmission electron micrographs (TEM) taken from microtomed hematite powders embedded in a polymer resin (Figure 4.1b-c). Here, particles sliced lengthwise clearly reveal densely packed crystallites with a preferred orientation. The lattice fringes of individual crystallites can also be visualized (Figure 4.1d) by using a high-resolution TEM. Planes were indexed with the Bravais-Miller hexagonal indices (hkil) due to the more intuitive usage, though hematite is a rhombohedral crystal with the *R3c* space group (a = 5.0356 Å, c = 13.7489 Å). Fig. 1e shows the selected area electron diffraction (SAED) pattern for the image presented in Figure 4.1c. Strong Debye arcs in both the $\{0\bar{1}12\}$ and $\{10\bar{1}4\}$ reflections suggest a pronounced texture consistent with the observed ordering of the acicular crystallites. During the microtoming process, peanut-shaped particles were also cut across the waist in a direction perpendicular to

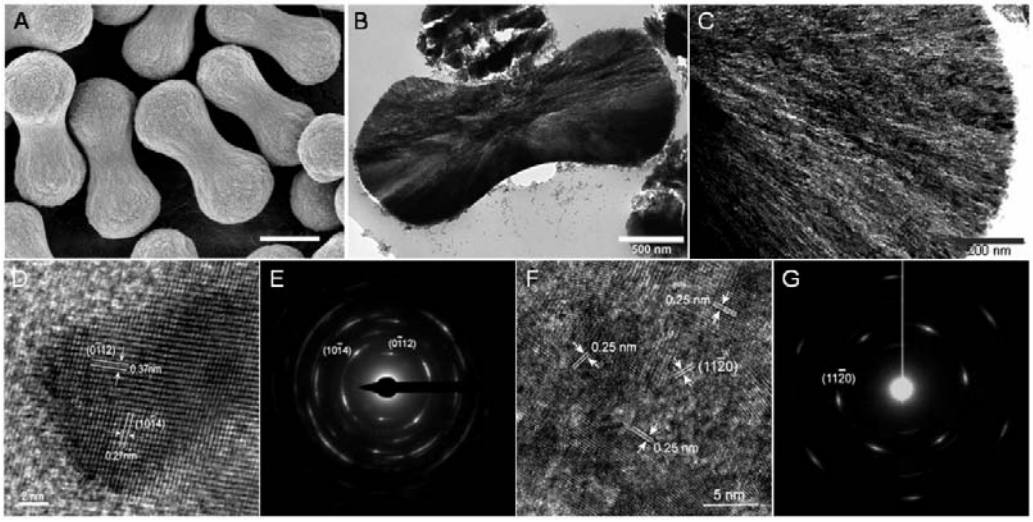

Figure 4.1. A) FE-SEM image of monodisperse hematite peanut-shaped colloids. Scale bar, 1 micron. B-C) TEM micrograph of a hematite particle (side view), illustrating the radial splay of acicular crystallites in the lobes. D) HR-TEM micrograph (side view) of a single crystallite at the very edge of a lobe. E) SAED pattern from the region shown in C. F) HR-TEM micrograph (axial view) taken from a colloid cut perpendicular to the particle major axis and G) its corresponding SAED pattern. The six-fold symmetry in the axial view suggests that the c-axis of hematite is collinear with the particle major axis.

the axis of revolution. A HRTEM micrograph (Figure 4.1f) from these particles displays polycrystalline grains with the $\{11\bar{2}0\}$ lattice spacing, while the corresponding SAED pattern (Figure 4.1g) shows the six-fold symmetry expected from a perspective down the hexagonal *c-axis*. Taken together, these results indicate that the major axes of the crystallites coincide with the hematite *c-axis*, and by extension, that peanut-shaped colloids possess an 'overall' crystalline orientation, such that the particles' major axes also coincide with the hematite *c-axis*.[15]

The main features of the α-Fe_2O_3 colloidal structure and magnetic ordering are highlighted in a schematic as illustrated in Figure 4.2. In this representation, only a thin plane of loosely packed and oriented crystallites (shown as blue spindles) are rendered for visual clarity. Hematite crystallizes in the corundum structure, in which oxygen anions lie on a hexagonally close-packed lattice (dotted line) and iron cations (red spheres) symmetrically occupy two-thirds of the octahedral interstitial sites. Its structure is slightly distorted from the ideal, in that some Fe cations lie above the hexagonal basal plane while others lie below it. Thus, the four nearest neighbor iron cations of an oxygen anion do not form a regular tetrahedron.[16] In terms of the magnetic structure Fe cations are ferromagnetically-ordered within each basal plane, but coupled in a (+ – – +) arrangement between planes to yield net antiferromagnetic behavior. A notable feature of hematite is that it undergoes a magnetic phase transition above the Morin temperature ($T_M \sim 263$K) into a weakly ferromagnetic state. As such, hematite exhibits a non-zero spontaneous magnetization perpendicular to its *c-axis* between $T_M < T < T_N$ (Néel temperature, $T_N \sim 953$K) due to canting of the magnetic spins away from the [0001] direction toward the basal plane. For the peanut-shaped colloids, canting produces a permanent dipole moment[17] oriented in a transverse direction to the particle major axis at room temperature. This unusual magnetic

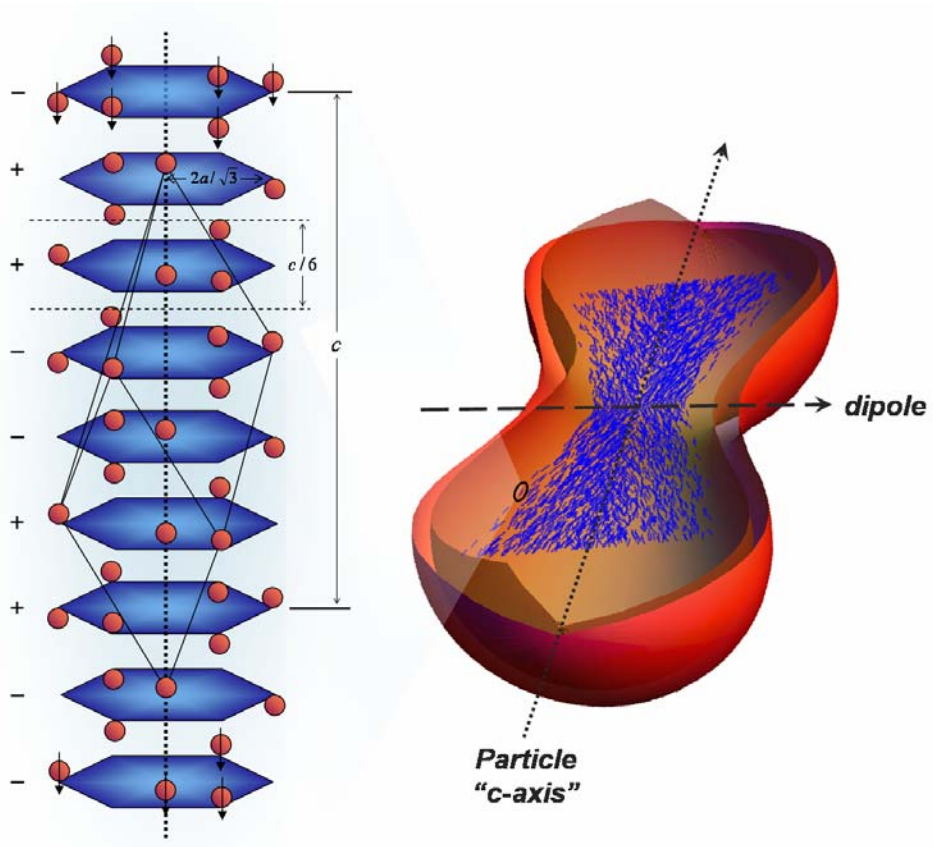

Figure 4.2. A schematic (left) showing the crystal structure (corundum) of a single crystallite of hematite (after ref [17]). Dotted lines represent planes of oxygen anions (not shown) while red spheres indicate the positions of the iron cations. Both the rhombohedral unit cell and the equivalent hexagonal system representation are shown. The black arrows illustrate the magnetic spin orientations in each plane (ordered in a + - - + fashion) below the Morin transition ($T_M \sim 263K$), when hematite is strictly antiferromagnetic. (Right) A schematic illustrating the core-shell peanut-shaped colloids and the hematite microstructure derived from aggregates of acicular crystallites (blue spindles). The particle's 'overall' *c-axis* is in the longitudinal direction, while the magnetic dipole moment (at $T > T_M$) is in the perpendicular i.e. transverse, direction.

anisotropy is a direct result of the particle microstructure, and plays a critical role in determining the colloidal structures that arise in both 1D and 2D.

An example of the complex structures formed by the peanut-shaped colloids is shown in the FE-SEM image of Figure 4.3a. Here, we coated hematite cores (zeta potential, $\zeta \approx$ -26 mV) with a thin layer of silica (48 nm) for charge stabilization ($\zeta \approx$ -46 mV), since they irreversibly aggregated from strong dipolar attractive forces otherwise. The sample was prepared by drying a dilute particle suspension (volume fraction, $\phi \sim 1 \times 10^{-3}$) on a silicon substrate in the presence of a neodynium bar magnet. In the resulting chains, peanut-shaped colloids formed random crisscrosses linked to adjacent particles primarily at the waist, and always along the short axes of the particles i.e., configured side-by-side. The orientation of the chain was parallel to the applied field, in agreement with previous reports of ordering in spherical MR fluids. For two fixed dipole moments at large separations, the interaction energy (ignoring multipole terms)[3] can be written as:

$$U_{dipole}(r,\theta) = \frac{m^2}{4\pi\mu_o} \cdot \frac{1-3\cos^2\theta}{r^3} \qquad (1)$$

where m is the magnetic dipole moment [2.4×10^{-21} AHm] per particle, μ_o is the permeability of free space [$4\pi \times 10^{-7}$ H/m], θ is the angle between the dipole orientation and a line joining the particle centers, and r is the dipole-dipole separation [m]. This magnetic energy is minimized when the dipoles are arranged head-to-tail (θ = 0) at close proximity, and thus favors the close-packed crisscross structure, in which the transverse dipoles need simply to rotate about the particle revolutionary axis to form the desired head-to-tail state. To estimate U_{dipole} in the peanut-shaped colloids, the field-dependent magnetization curve of the hematite powder was measured using a superconducting quantum interference device (SQUID) at 298 K (supporting

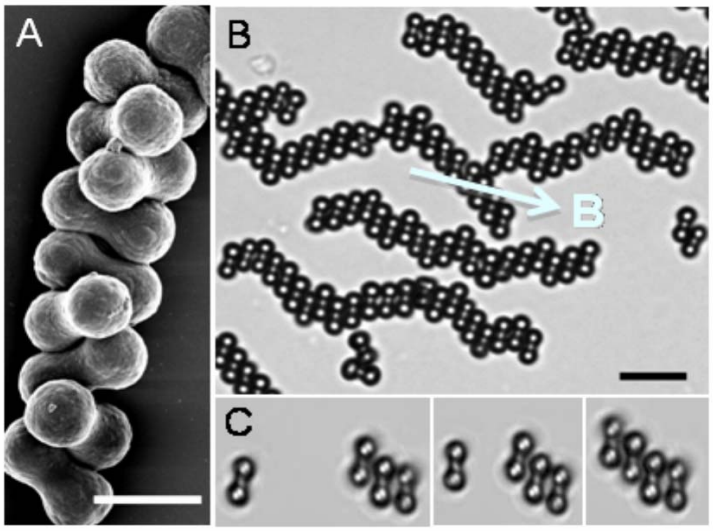

Figure 4.3. A) FE-SEM image of particle chains formed upon drying in a random crisscrossed configuration. Scale bar, 2 microns. B) Optical transmission micrograph of planar, kinked zigzag chains under 2D confinement. Scale bar, 5 microns. C) Time snapshots illustrating the growth of a linear close-packed aggregate ($N = 3$) by the addition of a new particle along the chain direction at (from left to right) $t = 0$, 10m 30s, and 10m 50s.

materials). The peanut-shaped colloids exhibit ferromagnetic behavior characterized by a coercivity of $H_c \sim 2500$ Oe and a remanence of $M_r \sim 0.19$ emu/g. Using equation (1), the maximum magnetic contribution to the pair potential is $U_{dipole} \approx -325\ k_BT$ for the crisscrossed structure at contact. In practice, this value is likely to be smaller due to thermal fluctuations (Brownian motion) that persistently cause the particle-particle orientations to misalign. At close range, the total interaction energy should also become increasingly dependent on the electrostatic, van der Waals, and local magnetic field effects i.e., $U_{total} = U_{dipole} + U_{chains} + U_{elec} + U_{VDW}$. It is worth noting that the use of anisometric particles introduces additional complications to evaluating the individual contributions to U_{total} based on the colloidal pair configuration i.e., crisscrossed, T-type, end-to-end, or side-by-side. Moreover, it has been suggested that confinement can cause anomalous potentials of a weak attractive nature ($\sim 1\ k_BT$), even in highly-charged colloids.[18]

To explore the structures that form in 2D, we restricted the peanut-shaped particles to planar geometries using a confinement cell[19] and observed the colloids in real-time using optical microscopy and videography. Figure 4.3b illustrates kinked zigzag chains (surface fraction, $\sigma \sim 0.16$) of the nonspherical particles assembled only under the geomagnetic influence. This inherent field is weak (~0.3 Oe) but provides a uniform intensity over an area well beyond the size of the confinement cell. As before, particles contact adjacent neighbors side-by-side, and the chain directions (averaging over kinks) are aligned with the Earth's field. If an oscillating magnetic field is applied, both individual particles and chains rotate in response. In the latter case, long chains dissociate into smaller rotating segments and quickly re-form upon removal of the external field. Applying a magnetic gradient also causes peanut-shaped particles to drift with their major axes perpendicular to their trajectory i.e., broad side on, in spite of the increased viscous drag. Videos of these two responses are included in the

supporting materials. Within the chains, particles remain Brownian and display conformational changes between the two preferred close-packed sites by transitioning through an open-packed rectangular arrangement. Such positional ordering was not observed in dipolar chains of pseudocubic and ellipsoidal hematite particles,[17] and underscores the important role of shape programming and complementarity on the self-assembly of colloidal building blocks. Figure 4.3c shows a series of time snapshots illustrating the growth of a chain (length $N = 3$) via addition of a free particle at one of the dangling ends. This side-by-side interaction was highly selective and zigzags grew to large N without significant chain-chain aggregation. The center-to-center equilibrium separation (R_c) of the peanut-shaped particles was measured to be 1.31 ± 0.09 μm, compared to the closest packing value (1.26 μm) calculated from the particle dimensions based on SEM images.

Zigzag aggregates were quantitatively analyzed with respect to the particle positional and orientational order, as well as the free energy in each of the chain bonds. Figure 4.4a shows the calculated radial distribution function for the zigzags using *xy*-coordinates from the particle centers. The *x-axis* was normalized by R_c so that integer multiples corresponded to occurrences of close-packed particles along a direction without any kinks. For example, a linear close-packed chain with $N = 3$ should have peaks located at R_c and $2R_c$ while a V-shaped chain with one kink should have peaks at R_c and approximately $\sqrt{3}\,R_c$. Split peaks at both the second and third nearest-neighbor distances (Figure 4.4a) thus reflect the high probability of finding kinks in this system. In Figure 4.4b the misorientation between the particles' major axes to the geomagnetic field direction is plotted in a histogram. The distribution is normal with a standard deviation of 7.8°. The alignment in the sample was also characterized by computing the nematic order parameter, *S*, based on the second Legendre polynomial:

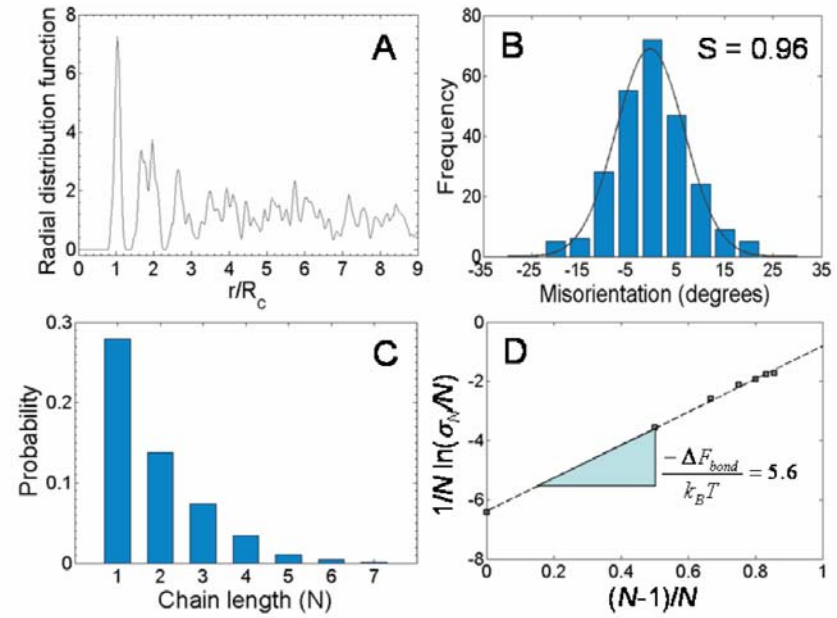

Figure 4.4. A) Radial distribution function of the particle chains based on their centers. B) Misorientation of particles with respect to the geomagnetic field (standard deviation, 7.8°). The nematic orientational order parameter was calculated to be $S = 0.96$. C) Chain length distribution in a dilute suspension ($\sigma_{avg} \sim 0.05$). D) Plot of $(1/N)\ln(\sigma_N/N)$ vs. $(N\text{-}1)/N$ from the data presented in C (squares). The slope of the best linear fit yields ΔF_{bond}, the free energy of a bond between two particles.[21]

$$S = \left\langle \frac{3\cos^2\theta - 1}{2} \right\rangle \qquad (2)$$

where θ is the misorientation angle. For the zigzag structures $S = 0.96$, compared to a theoretical value of 1 for a perfectly aligned particle system. To estimate the free energy of a bond in the chain (i.e., corresponding to U_{total}), a simple linear aggregation model was applied to the probability distribution of N-mers as a function of N (Figure 4.4c) in a dilute regime ($\sigma_{avg} \sim 0.05$). This model is exact in the limit of reversible chains interacting with nearest-neighbor attractions only,[20] and can be understood in terms of the equilibrium between particles in the monomeric state with particles in the N-mer state such that:[21]

$$N \text{ monomer} \leftrightarrow 1\ N\text{-mer} \qquad (3)$$

$$K = \frac{\sigma_N / N}{\sigma_1^N} = \exp\left[-(N-1)\frac{\Delta F_{bond}}{k_B T}\right] \qquad (4)$$

where K is the equilibrium constant, ΔF_{bond} is the change in the Helmholtz free energy associated with a single bond [J], N is the chain length, σ_N and σ_1 are the surface fraction of particles in an N-mer and monomer, respectively, k_B is Boltzmann's constant [1.38×10^{-23} J/K], and T is the temperature [K]. For the peanut-shaped magnetic particles, mild perturbations in the solvent flow were sufficient to break the aggregated zigzags. Additionally, Brownian motion within chains suggested that thermal energy could translate and rotate the particles. These indicators were therefore taken as qualitative demonstrations of reversibility in the system. As shown in Figure 4.4d, $(1/N)\ln(\sigma_N / N)$ was plotted as a function of (N-1)/N to extract the free energy of a single bond from the slope of the best linear fit (*-5.6 k_BT*). For comparison, chains of cylinders induced by the depletion effect had calculated free energies of *-4* to *-9 k_BT*,[21] while the onset of aggregation is generally not expected in colloidal systems until

potential wells reach *-3 k_BT* in depth.[22]

The combined anisotropic morphology and directional interactions make these particles interesting candidates for the assembly of colloidal analogues to molecular crystals.[13] As a simple demonstration, we show the potential to drive these building blocks into oblique 2D structures at high surface fraction. Figure 4.5a presents an optical transmission micrograph of a nearly dense monolayer ($\sigma \sim 0.72$) of oriented particles formed by the coalescence of individual zigzag aggregates. Crystallites are separated by voids due to kink mismatches, and can coarsen only when gaps are eliminated through particle rearrangements. Although such events occur with low probability (due to the stability imparted by a bond free energy of *-5.6 k_BT*), 'annealing' does occur on fairly reasonable time scales, with one example shown in a video in the supporting materials. Because the peanut-shaped particles are magnetically-responsive, it may also be possible to anneal the monolayers using magnetic field assisted means i.e., to thermalize the system, rotate particles, or induce short range transport. Some of the common defect structures found in the system are shown in Figure 4.5b-c. These typically comprise point defects, such as vacancies (of one particle lobe), or line defects (of a missing row of particle lobes). In addition, kinked lines within crystallites can be thought of as twin boundaries (see rearrangement movie, supporting materials). In Figure 4.5d, the oblique lattice (a = 1.33 ± 0.06 μm, b = 2.82 ± 0.13 μm) adopted by the oriented particles is clearly illustrated by an overlaid double cell. The interaxial angle γ was measured to be 122.0° ± 2.6°. A fast Fourier transform (FFT) of the region surrounding this crystallite is shown in Figure 4.5e. Well-defined low order spots are apparent, and the 2-fold rotational symmetry about the FFT origin confirms the oblique geometry from the *p2* plane group. We note that assembly of the anisotropic peanut-shaped colloids without 2D confinement resulted in a disordered

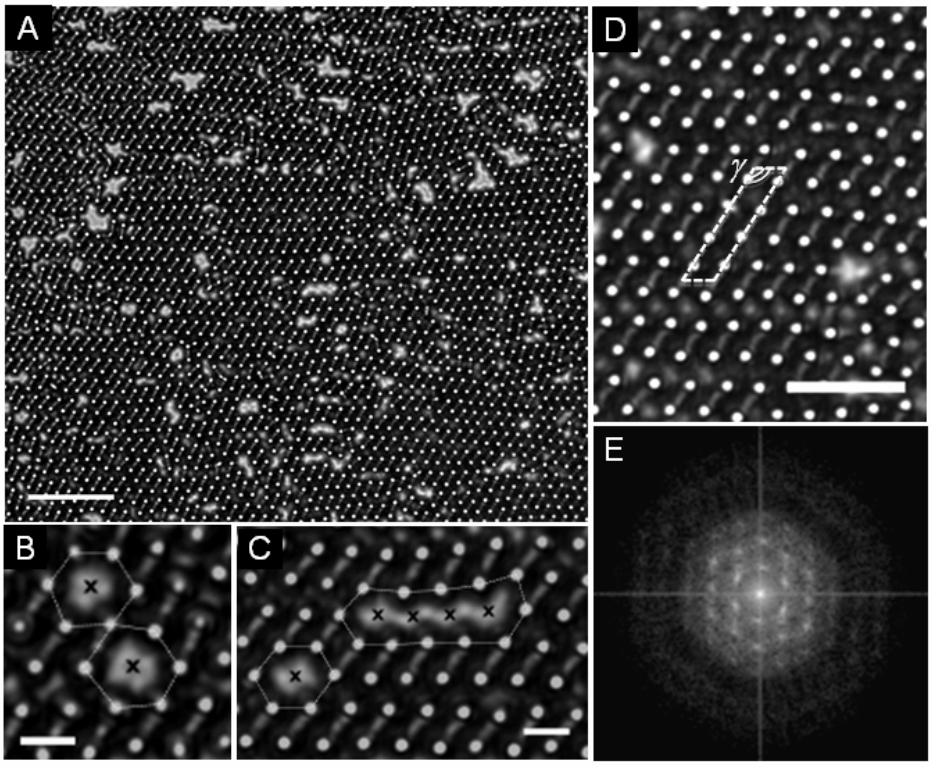

Figure 4.5. A) Optical micrograph of a nearly-dense monolayer of the peanut-shaped colloids. Individual particle orientations can be inferred from the grey lines connecting the two white circular lobes. Scale bar, 10 microns. B-C) Typical defect sites formed by the coalescence of zigzag chains. Two adjacent vacancies (marked by a black 'x') are illustrated in B, along with a vacancy close to a row of missing particle lobes in C. Highlights (white dotted line) were added to guide the eye. Scale bar, 2 microns. D) Close-up image of a crystallite, showing a double cell of the oblique lattice (a = 1.33 μm, b = 2.82 μm; γ = 122.0°) assumed by the oriented nonspherical particles (white overlay). Scale bar, 5 microns. E) FFT spectrum of the region shown in D. Low order spots are clearly visible, while the 2-fold rotational symmetry about the origin accurately reflects the real space structure from the *p2* plane group.

structure in 3D. Although particles within each chain assumed the random crisscrosses configuration (as shown in Figure 4.3a), there were little translational or orientational correlations found between the oriented chains.

In summary, this report demonstrates that magnetic peanut-shaped colloids can be driven into complex 1D and 2D structures by the balance of dipolar, electrostatic, and entropic (confinement) forces. Due to their size, these particles allow quantitative, real-time analysis of equilibrium structures on a single particle level. The particle geometry also enables peanut-shaped building blocks to close-pack, and thus organize into oblique molecular-type crystals and positionally-ordered zigzag chains in 2D. The magnetic dipoles in the colloids are a consequence of the hematite shape and microstructure, and impart directional interactions to the particle pair potential. A striking implication of this magnetic anisotropy is the high degree of selectivity in the side-by-side interaction. Another effect is the formation of orientationally-ordered monolayer structures, in contrast to our earlier report of an aperiodic crystal made from hollow peanut-shaped colloids without the magnetic hematite core.[19] The development of uniform colloidal particles with complexity in both shape and interactions should ultimately enable significant advances in fundamental colloid science and applications such as photonics.

Acknowledgements

This work was supported by a National Science Foundation Career Award No. DMR-0547976 and was performed in part at facilities of the Cornell Center for Materials Research (NSF MRSEC, DMR-0520404) and the Cornell Nanobiotechnology Center (NSF Agreement No. ECS-9876771). The authors thank J. Cha for high-resolution TEM imaging, M. Kamperman for microtoming, D. Loh for graphics assistance, and S. Badaire and J. Savage for insightful discussions.

Experimental

Particle Synthesis: Peanut-shaped α-Fe_2O_3 particles were synthesized via the gel-sol method[15] under hydrothermal conditions as follows: 2.0 M $FeCl_3$ (Mallinckrodt, 50 mL), 6.0 M NaOH (Aldrich, 45 mL), and 0.6 M Na_2SO_4 (Aldrich, 5 mL) were mixed and aged in an oven at 100 ºC for 8 days. Particles were then washed in deionized water (Millipore, 18.2 MΩ-cm), recovered through filtration, and stored as a loose powder. To coat the core hematite with a silica shell, 0.4 g of the α-Fe_2O_3 powder was dispersed in a mixture of 84 mL isopropyl alcohol (Aldrich), 12 mL ammonia solution (Mallinckrodt, 27%), 4 mL deionized water, and 180 μL tetraethyl orthosilicate (Aldrich, 98%). The suspension was sonicated (12-14W; Sonics & Materials, Inc. VCX-500) for 2 hours at a constant temperature of 30 ºC. At the end of the reaction particles were washed in deionized water before use in further experiments. To determine the particle dimensions at least 100 particles (polydispersity < 5%) were measured using SEM images.

Colloid characterization: Samples were characterized using field emission scanning electron microscopy (FE-SEM; Zeiss-1550), transmission electron microscopy (TEM; FEI Tecnai T-12 / 120 kV, and HRTEM; FEI Tecnai F-20 / 200 kV), and selected area electron diffraction (SAED; FEI Tecnai T-12, F-20). Magnetic hysteresis data was collected at 298 K using a superconducting quantum interference device (SQUID; Quantum Design MPMS-XL). The remanence value obtained (0.19 emu/g) was used to calculate the dipole moment per particle. For zeta potential values, measurements were made using dilute dispersions ($\phi \sim 3 \times 10^{-4}$) at 25 ºC (Malvern ZetaSizer Nano-ZS).

Assembly of particles in 1D, and 2D: Dried chains of silica-coated hematite colloids were organized under the slow evaporation of a dilute particle suspension ($\phi \sim 1\times10^{-3}$) on a silicon substrate, during which a neodymium bar magnet (850 Gauss) was placed approximately 2 mm from the edge of the droplet. For 2D experiments, peanut-shaped particles ($\phi \sim 3 \times 10^{-4}$) were confined between two glass slides with a wedge-like geometry.[19] Prior to use, the glass was washed in base (2:3 mixture of 6.25 M NaOH : ethanol), rinsed with deionized water, and dried. Zigzag chains were observed in real-time using an inverted optical transmission microscope (Zeiss AxioVert; 100x oil immersion lens, N.A. 0.55) equipped with an AxioCam MR3 camera. To analyze the chain length distribution, data was taken after suspensions were equilibrated in the wedge cells for ~3 weeks. Chain lengths were counted manually from the optical images, and the positions / orientations of individual colloids were determined using a custom Matlab routine with user-supplied mouse input. To increase surface fraction in the dense monolayers, filled confinement cells were tilted at an angle of approximately 75° (from horizontal) overnight to sediment the particles. Cells were allowed to equilibrate horizontally for at least 30 minutes before data acquisition. No signs of drift or a net flux of particles were observed in the region of interest. Angles and lattice vector magnitudes for the 2D oblique cell, as well as the FFT pattern, were obtained using ImageJ software. A circular mask (850 μm^2) was applied to the real space image in the latter prior to taking the transform.

APPENDIX

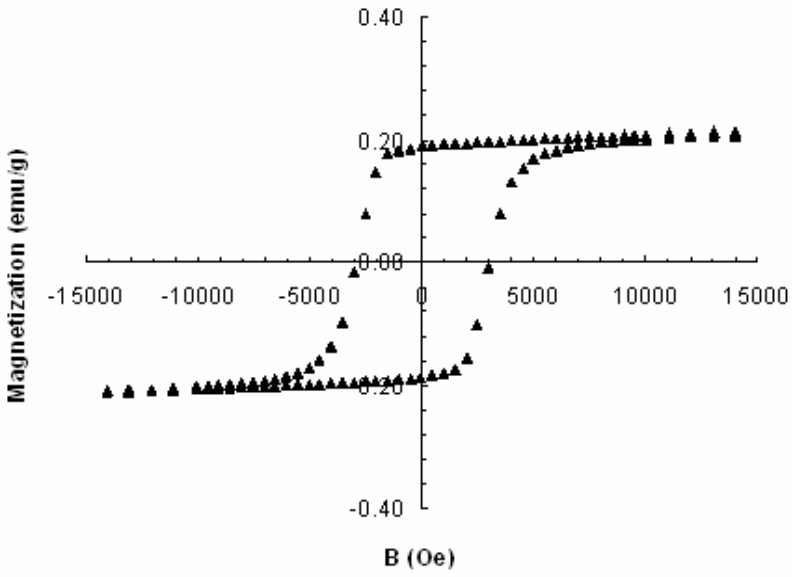

Figure 4.S1. SQUID measurement of the field-dependent magnetization of hematite peanut-shaped colloids at 298 K.

REFERENCES

1. P. C. Scholten. *IEEE Transactions on Magnetics*, **Mag-11**, 1400 (1975).

2. N. Minc, C. Futterer, K. D. Dorfman, A. Bancaud, C. Gosse, C. Goubault and J. L. Viovy. *Analytical Chemistry*, **76**, 3770 (2004).

3. E. M. Furst and A. P. Gast. *Physical Review E*, **61**, 6732 (2000).

4. M. R. Jolly, J. W. Bender and J. D. Carlson. *Journal of Intelligent Material Systems and Struct*ures, **10**, 5 (1999).

5. (a) W. Wen, L. Zhang and P. Sheng. *Physical Review Letters*, **85**, 5464 (2000). (b) W. D. Ristenpart, I. A. Aksay and D. A. Saville. *Physical Review Letters*, **90**, 128303 (2003). (c) I. Varga, H. Yamada, F. Kun, H.G. Matuttis and N. Ito. *Physical Review E*, **71**, 041505 (2005).

6. A. P. Hynninen and M. Dijkstra. *Physical Review Letters*, **94**, 138303 (2005).

7. A. Yethiraj and A. van Blaaderen. *Nature*, **421**, 513 (2003).

8. (a) S. M. Yang, S. H. Kim, J. M. Lim, G. R. Yi. *Journal of Materials Chemistry*, **18**, 2177 (2008). (b) C. M. Liddell and C. J. Summers. *Advanced Mater*ials **15**, 1715 (2003). (c) D. Nagao, M. Hashimoto, K. Hayasaka and M. Konno, *Macromolecular Rapid Communications*, **29**, 1484 (2008).

9. J. Q. Cui and I. Kretzschmar. *Langmuir*, **22**, 8281 (2006).

10. J. W. Kim, R. J. Larsen and D. A. Weitz. *Journal of the American Chemical Society*, **128**, 14374 (2006).

11. S. Gangwal, O. J. Cayre and O. D. Velev. *Langmuir*, **24**, 13312 (2008).

12. (a) D. K. Hwang, D. Dendukuri and P. S. Doyle. *Lab on a Chip*, **8**, 1640 (2008). (b) S. H. Lee, Y. Song, I. D. Hosein and C. M. Liddell, *Journal of Materials Chemistry*, **19**, 350 (2009). (c) S. K. Smoukov, S. Gangwal, M. Marquez and O. D. Velev. *Soft Matter*, DOI: 10.1039/b814304h (2009).

13. (a) C. Reichhardt, C. J. Olson. *Physical Review Letters*, **88**, 248301 (2002). (b) M. Brunner, C. Bechinger. *Physical Review Letters*, **88**, 248302 (2002).

14. T. Sugimoto, M. M. Khan and A. Muramatsu. *Colloids and Surfaces A - Physicochemical and Engineering Aspects*, **70**, 167 (1993).

15. D. Shindo, G. S. Park, Y. Waseda and T. Sugimoto. *Journal of Colloid and Interface Science*, **168**, 478 (1994).

16. A. H. Morrish. Canted antiferromagnetism: Hematite (World Scientific Publishing Company, 1994).

17. (a) M. Ozaki, H. Suzuki, K. Takahashi and E. Matijevic. *Journal of Colloid and Interface Science*, **113**, 76 (1986). (b) M. Ozaki, T. Egami, N. Sugiyama and E. Matijevic. *Journal of Colloid and Interface Science*, **126**, 212 (1986).

18. Y. Han, D. G. Grier. *Physical Review Letters*, **91**, 038302 (2003).

19. S. H. Lee, S. J. Gerbode, B. S. John, A. K. Wolfgang, F. A. Escobedo, I. Cohen and C. M. Liddell. *Journal of Materials Chemistry*, **18**, 4912 (2008).

20. M. Klokkenburg, R. P. A. Dullens, W. K. Kegel, B. H. Erne and A. P. Philipse. *Physical Review Letters*, **96**, 037203 (2006).

21. S. Badaire, C. Cotton-Bizonne and A. D. Stroock. *Langmuir*, **24**, 11451 (2008).

22. F. M. van der Kooij, M. Vogel and H. N. W. Lekkerkerker. *Physical Review E,* **62**, 5397 (2000).

CHAPTER 5

ASYMMETRIC COLLOIDAL DIMER ASSEMBLIES UNDER QUASI-2D CONFINEMENT

Abstract

The synthesis and assembly of mildly-fused asymmetric polystyrene/silica dimers confined to gap heights intermediate to an in-plane monolayer and an out-of-plane monolayer are explored. Using real-space confocal microscopy, we show that structures evolve from an oblique 2D phase to a quasi-2D rotator, and finally to an upright hexagonally-close-packed monolayer. The existence of the novel quasi-2D state i.e., where out-of-plane motion is allowed, highlights the critical role that confinement dimensionality plays on the nature of ordering in complex colloidal systems.

* Submitted as: Stephanie H. Lee and Chekesha M. Liddell. "Asymmetric colloidal dimer assemblies under quasi-2D confinement" (2009).

The assembly of microscopic nonspherical particles (300 nm to ~1 μm) has attracted recent interest, both from a fundamental standpoint, i.e., nucleation and growth, defect dynamics, and phase transformations in small molecule analogs; as well as from a technological perspective i.e., light control in optical applications, or elasticity in biomimetic composites.[1] A central challenge to such pursuits is the difficulty in producing and understanding the formation mechanisms of desirable structures by consistent, flexible, and controlled assembly methods.[2] Another challenge lies in synthesizing a broad palette of appropriate particles (i.e., in shape, size, monodispersity, or selective functionalities) in sufficient quantities.[3] Despite the apparent complexity, computational models have suggested that nonspherical building blocks are capable of forming diverse structures ranging from liquid crystalline phases and degenerate aperiodic crystals, to rotator or plastic crystals.[4-8] In the purview of reports which reveal that remarkable properties can be derived from partially-ordered and amorphous systems[9,10] arises the trend to explore unconventional colloid-based phases as next-generation materials with novel auxetic, negative refraction, or photonic crystal superlensing behavior.[11]

Colloidal shapes that have received the most consideration to date center primarily on those with a close relationship to traditional spheres i.e., spherocylinders, and dimers constructed from two connected or overlapping spheres.[12-15] Assembly in these cases are well complemented by an already existing framework of theoretical studies that provide both insight and guidance to the types of structures expected in 3D.[5-8] For colloidal dimers, multiple geometric descriptors have been formulated to classify the particle morphology. These include the relative bond length, L^*, which expresses the degree of fusion between the two constituent lobes in a particle, and ($1-s^*$), which reflects the relative lobe anisotropy. We define $L^* = L/D_l$ and $s^* = D_s/D_l$, where L is the center-to-center distance between the lobes and D_l (D_s) is the diameter

of the larger (smaller) lobe. Large L^* values thus represent well-separated or mildly-fused dimers, while a $(1-s^*)$ value of zero corresponds to colloids that are completely symmetrical about their minor (short) axes.

Computational simulations based on hard spherocylinders of varying L^* have illustrated that this parameter is critical to the landscape of an equilibrium phase diagram. Specifically, for particles with $L^* \leq 0.35$ the system supports a plastic crystal (rotator) as a stable intermediate phase when the orientationally-ordered solid melts into an isotropic fluid.[5] Such a rotator is not observed between $L^* = 0.35$ and $L^* = 3.1$. The richness of phase space in the dimer system however, is not fully described by existing theoretical reports, particularly in 2D. For example, in nonspherical colloids there can conceptually be two types of monolayers: one in which the particles are lying flat (i.e., in-plane), and one in which they are standing upright (i.e., out-of-plane). Only the first scenario is considered in conventional 2D simulations. Much less attention has been focused as well on quasi-2D (Q2D) systems, although these most closely mimic the conditions commonly found in experiments. It is worth noting that Q2D confinement effects can lead to the assembly of buckled, layered, or rhombic-type structures.[16,17] In colloidal spheres, the introduction of small amplitude out-of-plane motions can also shift the phase boundaries predicted under the assumption of planar motion,[18] and stabilize an equilibrium hexatic phase with strongly first-order liquid-to-hexatic and hexatic-to-solid transitions.[19] A closer look at these systems may therefore extend, in a simple fashion, the types of phases available to nonspherical colloids.

The current report describes the synthesis and assembly of mildly-fused (i.e., high L^*) asymmetric polystyrene/silica (PS/SiO_2) dimers confined to glass cells with gap heights intermediate to the in-plane monolayer and the out-of-plane monolayer. Using real-space confocal microscopy, we show that structures evolve with increasing

gap height from a 2D (planar) oblique phase, to a Q2D rotator, and finally to a 2D (upright) hexagonally-close-packed crystal. The existence of this transition Q2D rotator is feasible only when strictly 2D conditions are relaxed i.e., by allowing for small out-of-plane motion.

Figure 5.1a shows a field-emission scanning electron microscope (FE-SEM) image of the uncoated asymmetric PS dimers [particle length, $H = 2.74$ μm; $L = 0.97$ μm, $D_l = 1.91$ μm, and $D_s = 1.63$ μm]. The particle shape anisotropy is characterized by L^* and (1-s^*) parameters of 0.51 and 0.14, respectively. PS colloids are decorated with a thin shell (65 ± 15 nm) of rhodamine isothiocyanate-labeled silica[20] to make them suitable for fluorescent imaging using a confocal laser scanning microscope. In optimizing the deposition, it was found that 3-aminopropyltriethoxysilane promoted the formation of the most conformal shells amongst the coupling agents tested (see supporting information). Thus, its usage led to smooth core-shell dimers with a morphology qualitatively similar to the original template (Figure 5.1b). L^* and (1-s^*) values were 0.49 and 0.11 after coating, as adding a uniform shell modifies the major and minor dimensions of a nonspherical object by different ratios. This geometrical concept can be exploited to continuously modulate the exact shape of dimer particles i.e., even ultimately converting it back to a sphere in the extreme case, by simply controlling the shell thickness.

The confinement cell used in the studies is designed with a wedge-like structure (Figure 5.1c), in which gap heights (h) corresponding to an in-plane particle monolayer (i.e., $h = D_l$), an out-of-plane monolayer (i.e., $h = H$), and the 3D case (i.e., $h > 100$ μm) are all present simultaneously within one cell. Particles are effectively confined between two hard parallel plates on a local length scale since the gap height varies only at a rate of ~1 μm/mm. To focus our studies on the regime where $D_l < h < H$, we slowly sedimented a density-mismatched dispersion of the dimer colloids at an

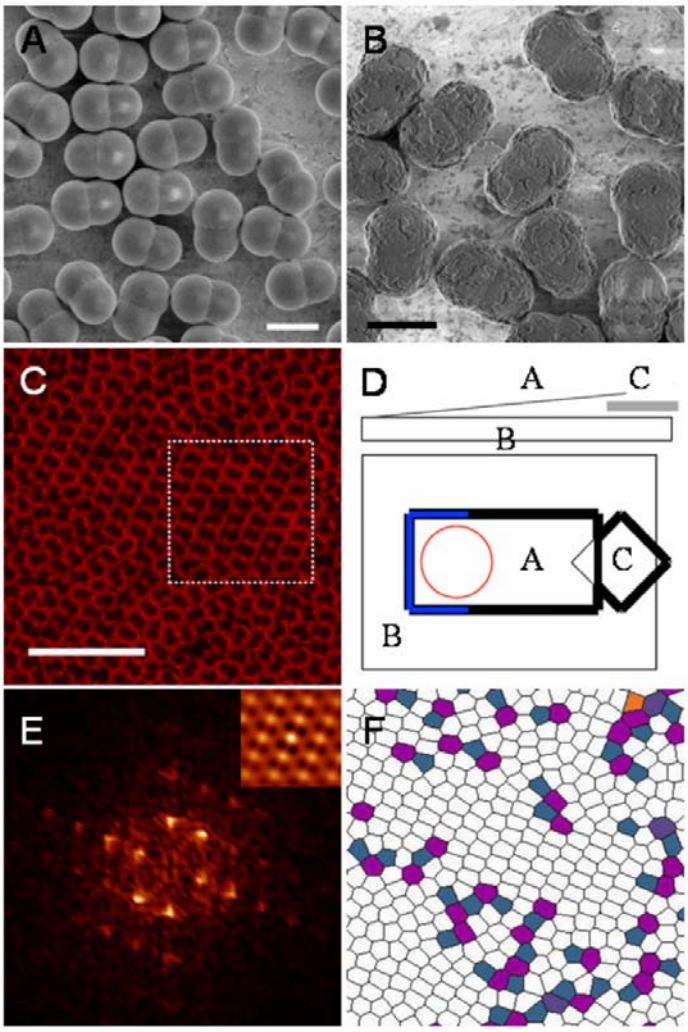

Figure 5.1. Monodisperse asymmetric PS dimers A) prior to the silica coating [L^*=0.51, $(1-\sigma^*)$=0.14] and B) after the fluorescent labeling [L^*=0.49, $(1-\sigma^*)$=0.11]. Scale bar, 2 microns. C) Confocal micrograph of a 2D oblique region when $h \approx D_l$. Scale bar, 15 microns. D) Wedge-type confinement cell. A is a thin coverslip, B is a microscope slide support base, and C is a spacer coverslip. E) FFT pattern of the oblique crystallite from C (hatched area), indicating two-fold symmetry. Inset, the autocorrelation function. F) Voronoi construction of the oblique region.

angle of ~10° over at least 120 hours, and verified that the system was equilibrated prior to data acquisition. To the best of our knowledge, there are currently no theoretical studies that directly address the complete 2D phase behavior of asymmetrical dimers between $0 \leq L^* \leq 1$. Nevertheless, 2D oblique crystals are likely to form at $L^* = 0.49$ with either the *c1m1* (parallel particle directors) or *p1* (antiparallel or random directors) plane group symmetries when $h \approx D_l$, if the 3D spherocylinder results described previously can be extrapolated to the 2D case. In the cell, small orientationally-ordered crystallites ($d_{avg} < 10$ μm) surrounded by a random matrix of densely packed dimers were found (Figure 5.1d; average surface fraction, $\sigma \sim 0.72$). A fast fourier transform (FFT) pattern (Figure 5.1e) taken from the hatched region marked in Figure 5.1d confirms that crystallites possess the two-fold symmetry characteristic of the oblique phase [$a = 2.06$ μm; $b = 2.87$ μm; interaxial angle = 68.5°]. To further illustrate these structural features, a Voronoi diagram (Figure 5.1f) portrays the elongated hexagonal geometry at each lattice site. Asymmetric dimers lacking six-fold coordination (i.e., disclination sites) are represented by colored tiles as a guide to visualize defects in the system. Grain coarsening and improved crystallinity were not observed in the oblique crystals even with subsequent annealing of up to 4 days. The calculated radial distribution function, *g(r)*, showed few distinguishable peaks, much like the curves generated from amorphous or liquid phases (see supporting info).

Another structure featured in the wedge cells was a solid (Figure 5.2a; $\sigma \sim 0.84$) bearing close resemblance to the 2D rotator formed by low L^* dimers at high surface fraction. Here, the colloidal centers-of-mass also lie approximately on a hexagonal lattice [$a = 2.56$ μm; $b = 2.57$ μm; interaxial angle = 60.6°], though confocal z-stack scans indicated that h was large enough with respect to D_l to allow particles to orient in random directions tilted *out* of the focal plane. The FFT,

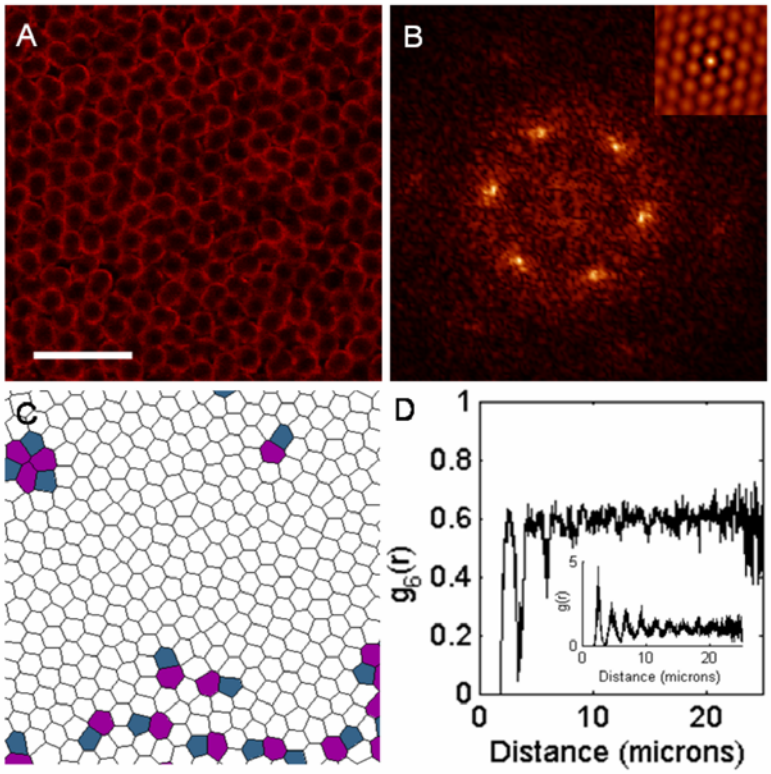

Figure 5.2. A) Confocal micrograph of a Q2D rotator region at $D_l<h<H$. Scale bar, 10 microns. B) FFT pattern of A, showing the characteristic six-fold symmetry. Inset, the autocorrelation function. C) Voronoi construction. D) The bond-orientational correlation function, $g_6(r)$, for the Q2D rotator. Inset, the radial distribution function, $g(r)$.

autocorrelation, and Voronoi construction (Figure 5.2b-c) reflect the six-fold symmetry of this Q2D state. Additionally, the computed *g(r)* revealed discrete peaks (Figure 5.2d) that persist to a long spatial range before reaching an asymptotic value of unity. To quantify the orientational symmetry, the bond-orientational correlation function, $g_6(r)$, was plotted in Figure 5.2d. The plateau value (~0.6) suggests a lower degree of local hexagonal order when compared to ideal crystals assembled from spheres [where $g_6(r) \rightarrow 1$], but is virtually identical to that of a 2D rotator dry film assembled from PS dimers with $L^* = 0.33$ and $(1\text{-}s^*) = 0.14$.[15] Observed grain boundaries ($d_{avg} \sim 20$ μm) are responsible, at least in part, for the decay of $g_6(r)$ over this distance. The extent to which this Q2D structure was expressed in the cell demonstrates the sensitivity dimers have to the availability of excess free volume.

At a gap height of $h \approx H$, the particles self-organized into an out-of-plane hexagonal monolayer (Figure 5.3a; $\sigma \sim 0.81$), as previously accomplished using heat-assisted convective assembly.[12] The FFT pattern and autocorrelation (Figure 5.3b) are consistent with a crystalline phase with *p6mm* plane group symmetry [$a = 2.18$ μm; $b = 2.18$ μm; interaxial angle = 59.3°], while the range of the distinctive spots indicate good spatial correlations. Analysis of the Voronoi construction (Figure 5.3c) reveals more regular hexagons than in the case of the Q2D rotator, as well as a reduced concentration of disclination defects. Thus, the small dimer lobe asymmetry does not appear to hinder crystallization of the hexagonal structure ($d_{avg} \sim 55$ μm). Significant long-range translational and orientational order can also be seen clearly in the *g(r)* and $g_6(r)$ functions (Figure 5.3d), particularly when considering the high plateau value in the latter (~0.85).

In this study, we explored the progression of colloidal structures formed by asymmetric PS/SiO_2 dimers confined to gap heights between a planar and an upright Monolayer. Striking, a novel Q2D rotator phase was observed at intermediate

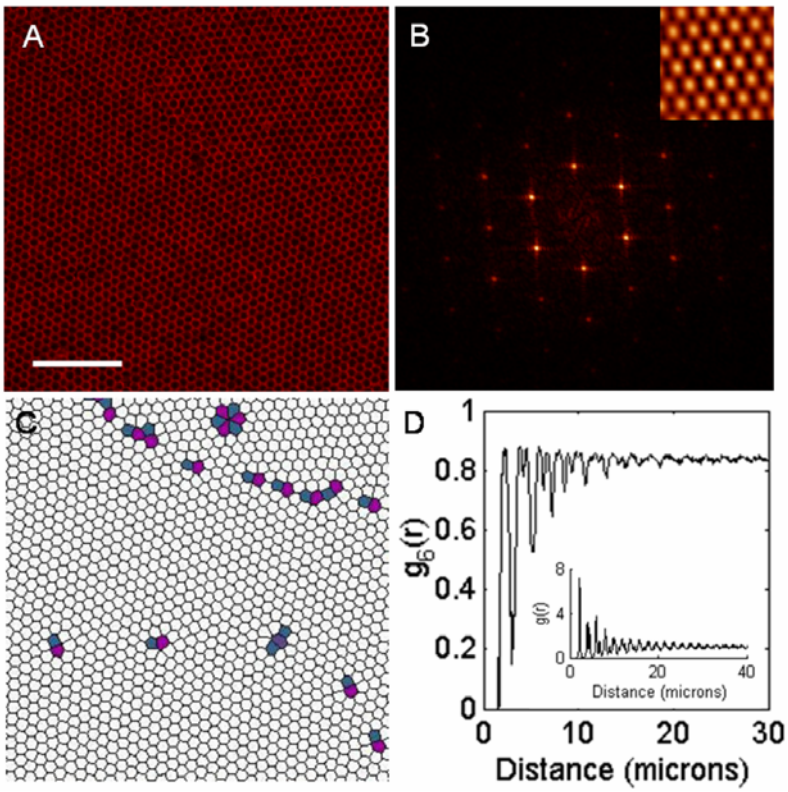

Figure 5.3. A) Confocal micrograph of an out-of-plane hexagonal monolayer at $h \approx H$. Scale bar, 20 microns. B) The corresponding FFT pattern, illustrating a high degree of crystallinity. Inset, the autocorrelation function. C) Voronoi construction. D) $g_6(r)$ and (inset) $g(r)$ curves.

heights upon relaxation of strictly 2D conditions. The existence of this state supports the idea that the nature and extent of ordering in a colloidal dispersion are strong functions of the confinement dimensionality. This same concept applies whether in the case of spherical particles,[16-19] or in broader molecular systems, such as in the mesostructured thin films formed by block copolymer melts.[21] The use of nonspherical particles, in combination with the variable gap height cell, is a versatile platform with which to investigate the rich behavior of novel colloidal suspensions. Removing the PS core to produce hollow dimers will also allow for refractive index matching (between the colloids and the fluid) so that extensions to the 3D case can be accessed. This effort is a focus of our ongoing research.

Acknowledgements

This work was supported by a Department of Energy Basic Energy Sciences grant award and performed in part at facilities of the Cornell Center for Materials Research (NSF MRSEC, DMR-0520404). We gratefully thank S. Gerbode and I. Cohen for experimental assistance and insightful discussion.

APPENDIX

Experimental

Particle Synthesis: Asymmetric PS core dimers were purchased from Magsphere Inc. (Pasadena, CA) and used as received. To enhance the silica compatibility to the PS surface, 167 mg of the core particles were mixed overnight with 9.5 mL absolute ethanol (Pharmco Inc.) and 500 μL 3-aminopropyltriethoxysilane (APS, Aldrich), before being isolated for the coating steps via centrifugation. Treatments with other coupling agents, such as triethoxy(octyl)silane and 3-trimethoxysilylpropyl methacrylate, were found to produce less consistent coatings and were therefore not used beyond the initial trials. Colloids were coated in a dynalene bath set at 30°C under constant sonication using an immersion probe (11-14 W; Sonics & Materials Inc. Model VCX-500). In a typical synthesis, PS dimers were added to 94 mL isopropyl alcohol (Aldrich) and 4 mL ammonia solution (27% v/v, Mallinckrodt), with aliquots of a sol-gel precursor injected each hour for a total of six additions. The additions consisted of 15 μL rhodamine isothiocyanate dye solution (900 μL APS, 250 mg dye, 10 mL absolute ethanol) and 30 μL tetraethylorthosilicate (TEOS) three times, followed by 45 μL TEOS three times. The mixture was sonicated overnight and washed via centrifugation. Dimers were re-coated, this time with non-fluorescently labeled silica. A single dose of 75 μL TEOS at the start of a 3 hour sonication period was used. Colloids were washed and treated with poly(vinylpyrrolidone) (PVP, 40000MW), before being re-dispersed into deionized water (18.2 MΩ-cm, Millipore).

Characterization: FE-SEM micrographs were acquired with a Zeiss-1550 field emission scanning electron microscope operating at 1 kV. Confocal images were obtained using a Zeiss LSM 5 LIVE inverted laser scanning confocal microscope (532

nm excitation). Based on the real-space confocal snapshots, the program WSxM (v3.0 Beta 7.5, Nanotec Electronica) was used to generate fast Fourier transforms and autocorrelation images. A custom Matlab routine determined the dimer positions from the confocal micrographs with user-supplied input. Analysis of the unit cell lattice vectors and angles were measured using ImageJ software.

Particle Assembly: The confinement cell was assembled from three affixed glass surfaces treated with PVP, which consisted of a 22 mm x 50 mm coverslip (No. 1½, VWR) positioned over a 1" x 3" microscope slide (VWR), and propped up at one end by a 22 mm x 22 mm spacer coverslip (No. 1, VWR). The cell was sealed using a combination of five minute epoxy and Norland UV glue along three sides, leaving the propped end available for sample injection. Approximately 50 μL of the dispersion was added with a pipette, after which the cell was completely sealed. To sediment the particles to the 2D and Q2D regions, cells were tilted at ~10° for at least three days prior to preliminary confocal data collection.

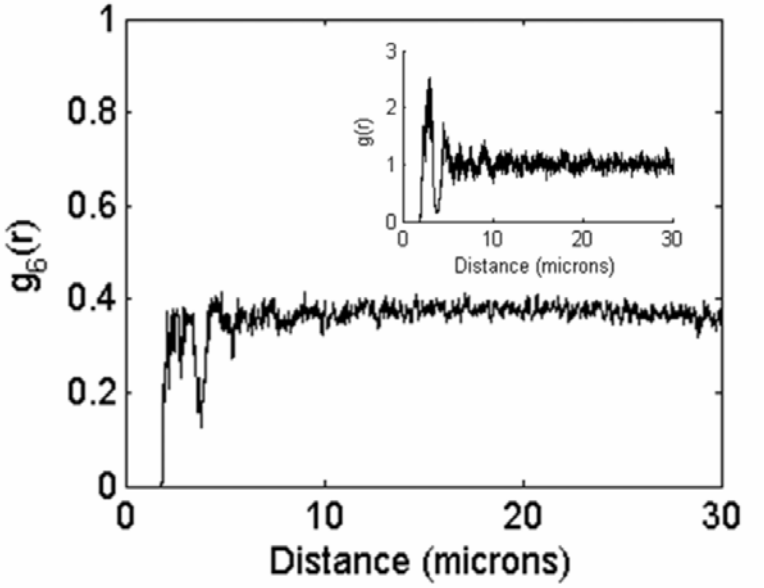

Figure 5.S1. The bond-orientational correlation function, $g_6(r)$, and (inset) radial distribution function, $g(r)$, curves for the 2D oblique structure.

REFERENCES

1. T. H. Lin, W. H. Huang, I. K. Jun and P. Jiang. *Electrochemistry Communications*, **11**, 14 (2009).

2. M. Maldovan, C. K. Ullal, W. C. Carter and E. L. Thomas. *Nature Materials*, **2**, 664 (2003).

3. S. M. Yang, S. H. Kim, J. M. Lim, and G. R. Yi. *Journal of Materials Chemistry*, **18**, 2177 (2008).

4. K. W. Wojciechowski, D. Frenkel and A. C. Branka. *Physical Review Letters*, **66**, 3168 (1991).

5. P. Bolhuis and D. Frenkel. *Journal of Chemical Physics*, **106**, 666 (1997).

6. C. Vega, E. P. A. Paras and P. A. Monson. *Journal Chemical Physics*, **96**, 9060 (1992).

7. B. S. John, A. Stroock and F. A. Escobedo. *Journal of Chemical Physics*, **120**, 9383 (2004).

8. M. Marechal and M. Dijkstra. *Physical Review E*, **77**, 061405 (2008).

9. K. Edagawa, S. Kanoko and M. Notomi. *Physical Review Letters*, **100**, 013901 (2008).

10. Z. Feng, X. Zhang, S. Feng, K. Ren, Z. Y. Li, B. Cheng and D. Zhang. *Journal of Optics A: Pure and Applied Optics*, **9**, 101 (2007).

11. K. V. Tretiakov and K. W. Wojciechowski. *Journal of Noncrystalline Solids*, **352**, 4221 (2006).

12. I. D. Hosein and C. M. Liddell. *Langmuir*, **23**, 10479 (2007).

13. S. H. Lee, S. J. Gerbode, B. S. John, A. K. Wolfgang, F. A. Escobedo, I. Cohen and C. M. Liddell. *Journal of Materials Chemistry*, **18**, 4912 (2008).

14. E. B. Mock, H. De Bruyn, B. S. Hawkett, G. S. Gilbert and C. F. Zukoski. *Langmuir*, **22**, 4037 (2006).

15. I. D. Hosein, B. S. John, S. H. Lee, F. A. Escobedo and C. M. Liddell. *Journal of Materials Chemistry*, **19**, 344 (2009).

16. P. Pieranski, L. Strzelecki and B. Pansu. *Physical Review Letters*, **50**, 900 (1983).

17. M. Schmidt and H. Lowen. *Physical Review Letters*, **76**, 4552 (1996).

18. D. Frydel and S. A. Rice. *Physical Review E*, **68**, 061405 (2003).

19. A. H. Marcus and S. A. Rice. *Physical Review E*, **55**, 637 (1997).

20. A. van Blaaderen and A. Vrij. *Langmuir*, **8**, 2921 (1992).

21. J. Fan, S. W. Boettcher, C. K. Tsung, Q. Shi, M. Shierhorn and G. D. Stucky. *Chemistry of Materials*, **20**, 909 (2008).